A Power-Efficient Radio Frequency Energy-Harvesting Circuit

by

Philip Khoury

A thesis submitted to the Ottawa Carleton Institute for Electrical and Computer Engineering
In partial fulfillment of the requirements for the degree of

Master of Applied Science

in

Electrical Engineering

Department of Electrical Engineering and Computer Science
Faculty of Engineering
University of Ottawa
Ottawa, Ontario, Canada
January 2013

Abstract

This work aims to demonstrate the design and simulation of a Radio Frequency (RF) energy-harvesting circuit, from receiving antenna to the point of charge collection. The circuit employs a custom-designed antenna based around Koch fractal loops, selected for their small physical size, good multiband behaviour and ease of size scalability, as well as a power-efficient seven-element Greinacher rectification section designed to charge a super-capacitor or rechargeable battery for later use. Multiple frequency bands are tapped for energy and this aspect of the implementation was one on the main focus points. The bands targeted for harvesting in this thesis will be those that are the most readily available to the general Canadian population. These include Wi-Fi hotspots (and other 2.4GHz sources), as well as cellular (850MHz band), Personal Communications Services (1900MHz band) and WiMax (2.3GHz) network transmitters.

Acknowledgments

I would like to thank Dr. Yagoub for his supervision efforts and guidance in the development of this thesis. Further, the faculty and staff at the University of Ottawa were instrumental in granting me access to the required facilities and resources.

Also, I would like to express my heartfelt thanks to my fiancée, Kateri, for her support and understanding throughout this thesis process.

Table of Contents

List of Figures

List of Tables

List of Symbols

Symbol	Definition of Use
Γ (gamma)	Reflection coefficient
ε (epsilon)	Permittivity
η (eta)	Efficiency
θ (theta)	Angle
λ (lambda)	Wavelength
ϕ (phi)	Angle
ω (omega)	Angular frequency
c	Free space velocity of light ($3x10^8$ m/s)

List of Acronyms

Acronym	Extended Terminology
AC	Alternating Current
AM	Amplitude Modulation
DC	Direct Current
DOI	Digital Object Identifier
FM	Frequency Modulation
GPS	Global Positioning System
PAE	Power Added Efficiency
PCB	Printed Circuit Board
PCS	Personal Communications Services
RF	Radio Frequency
RFID	Radio Frequency Identification
RSSI	Received Signal Strength Indicator
RX	Receiver
SMT	Surface Mount Technology
TX	Transmitter

Chapter 1 – Introduction

1.1 – Motivation

The number of consumer-oriented compact electronic devices (including, but not limited to, personal cellular phones, tablet PCs and GPS units) has been growing at exponential rates for several years. Reliance on these devices for daily navigation, scheduling and information-gathering activities has created an expectation of ever-longer battery life and less frequent charging cycles with any new generation of product. Consumers want to have full access to their devices' functionality without having to worry about whether or not they remembered to charge or change the associated batteries the night before.

This situation poses important questions to both design engineers and the originating vendors of these devices. How can we power these circuits in a responsible manner, while reducing wasted transmitted energy? How can engineers improve battery life and thus provide maximum 'up' time for consumers, with minimal interruptions for charging? Much of the work done towards answering these questions has involved reducing power draw and increasing application circuit power efficiency. After reaping the benefits of these efforts, an innovative next step in design evolution would be the minimization of the reliance on bulky and wasteful power sources, i.e. traditional high-capacity batteries. To sever this ‘cord’, the energy must come from some tangible and universally available source.

Many such sources of *ambient* energy are available for use by the aforementioned consumer devices: solar energy, wind energy, kinetic energy conversion and recycled ambient electromagnetic (EM) or Radio Frequency (RF) energy, to name a few. All of these concepts fall into the realm of so-called 'green' (or ecologically-friendly) power sources, which are becoming increasingly important from both environmental and marketing perspectives. The ever-growing spread of commercial and personal wireless installations focuses our attention on the collection of ambient RF energy emanating from cellular base

stations, Wi-Fi access points and dozens of other such sources. In short, as the industry grows, so will the number of potential power sources. It thus makes logical sense to target an energy source that seems likely to continue to grow over time.

The aim of this work is to aid the further development of consumer-oriented RF energy harvesting through an improved energy collection circuit with high power conversion efficiency and a newly modified compact circuit topology.

1.2 - Contribution

This thesis will explore the available means of RF energy harvesting and introduce elements for an improved collection circuit for implementation into an arbitrary electronic device with low power requirements, such as a handheld calculator or a wireless hygrometer/thermometer. The inclusion of multiple RF bands adds an opportunity for higher energy collection rates and thus faster charge accumulation.

The main contribution of this thesis remains on the design of a 'rectenna' circuit, comprised of a Koch fractal loop antenna, as well as a seven-element rectification section. The goal is to increase power conversion efficiency over similar recent designs and advance towards a workable solution that is efficient enough for market adoption in low power mobile devices. The bands targeted for harvesting in this thesis will be those that are the most readily available to the general Canadian population. These include Wi-Fi hotspots (and other 2.4GHz sources[1]), as well as cellular (850MHz, 900MHz bands), Personal Communications Services (1900MHz band) and WiMax (2.3GHz) network transmitters.

1.3 - Thesis Outline

In Chapter 2, an overview of the recent history of energy harvesting and a state of the art literature review of some important papers that are relevant to the harvesting of ambient RF

[1] Other 2.4GHz sources include, but are not limited to, microwave ovens, cordless phones, wireless alarm sensors and local mesh networks (such as ZigBee).

energy are presented. Selections for antenna and rectifier are then made, based on comparisons from literature. Chapter 4 focuses on an improved implementation, which comprises the bulk of this work. The result is a fully functional RF energy harvesting design containing a tuned antenna and signal rectification circuitry. Simulation results are then presented and explained, followed by a concluding chapter in which considerations for real-world implementation are discussed, as are shortcomings and areas for future improvement.

Chapter 2 – Background

2.1 – Energy-Harvesting Options

The advent of the battery-powered device has created an insatiable need for longer battery life and untethered device use. For example, one of the first cellular phones, the Nokia 1011, advertised a 'talk time' of 90 minutes on a fully-charged battery[2]. Today, current phones, such as the Sonim XP3300 Force[3] and the Samsung E2370[4] tout over 20 hours of 'talk time'. Steps have been taken to virtually rid the cellular phone of the need for recharging. Attempts have included kinetic energy harvesting, from phone movement, and solar energy. Unfortunately, the power required by modern cellular 'smart' phones still outweighs the energy produced by currently feasible implementations of these methods.

For devices with smaller current requirements, these harvesting schemes start to become viable. This factor, coupled with the attractive possibility of operating without worrying about recharging or replacing batteries, has helped to drive recent works in the field. The small, battery-powered electronics that this work aims to power include handheld calculators, wireless sensors (such as those measuring temperature and humidity) and small LCD clocks or timers. The next few paragraphs provide an overview of some common energy harvesting schemes targeting devices in the list above.

Solar energy, which involves converting the Sun's rays into useable electrical energy is interesting, but depends on the availability of daylight. The concept is certainly not foreign to the general population anymore. Solar-powered calculators and LED garden lights

[2] Spearmon, P. (n.d.). *Nokia Phones and Deals.* Retrieved April 2012 from http://www.articlesnatch.com/Article/Nokia-Phones-And-Deals/1393484

[3] (n.a.) Sonim Technologies Inc. 2011. *Sonim XP3300 Force Technical Specifications.* Retrieved April 2012 from http://www.sonimtech.com/pdf/XP3300_Force_Datasheet_EU_small.pdf

[4] (n.a.) Samsung . (n.d.) *Samsung E2370 – Caractéristiques du Produit.* Retrieved April 2012 from http://www.samsung.com/fr/consumer/mobile-phones/mobile-phones/businesss/GT-E2370FSAXEF/index.idx?pagetype=prd_detail

have been commonplace for many years now. The efficiency of such conversion circuits has grown, but the main detriment is the need for agreeable weather and timely use. Energy collection from natural sources at night is simply out of the question, limiting the user to daytime energy collection or requiring artificial sources of light with their own power supply needs. This method thus falls outside the scope of this work.

Wind energy, for its part, requires bulky turbines for collection and necessitates the inclusion of mechanical components and brushings that are susceptible to wear and damage over time, if not properly maintained. This is not an issue in traditional wind farm installations, where regular maintenance is expected to occur. The same expectation however cannot be placed on consumers and this energy source will thus not be further explored in this work.

Kinetic energy harvesting aims to transform motional or inertial energy into a usable source of electrical charge via some type of transducer. In general, this requires some physical effort by the user, be it walking, running or otherwise shaking the device. Though this is not a problem for most able-bodied people, it could nonetheless be considered a hassle for a device intended for daily use, such as a personal cellular phone or a GPS unit. This method will not be expanded upon in this paper.

Radio frequency energy, for its part, is readily available in all major industrialized centres and surrounding areas. The dramatic increase in demand for wireless devices has been met with a steady increase in infrastructure installations and thus an augmented source of radiated RF energy. This energy is in the air at virtually all times of the day and night, albeit at different power levels. A 2008 study [1] of ambient GSM power in the Netherlands concluded that within a range of 25-100m from a GSM basestation, the summed average power present at all measured frequencies across the 935-960MHz band varied between $0.1 mW/m^2$ and $3.0 mW/m^2$ and depended greatly on the amount of GSM traffic at the time of measurement. This in itself poses a potential problem for energy harvesting devices: the small amount of energy available for harvesting is neither constant nor easily predictable. As

such, one must ensure that any harvesting design remains useful over a wide dynamic range of available input power. Nonetheless, this form of ambient energy remains the most promising for use in consumer-oriented portable electronic devices, due to theoretical 24 hour availability, lack of required physical effort to charge and quasi-independence from weather conditions.

2.2 – Recent Development of RF Energy- Harvesting

Studies of wireless power *transfer* have occurred since the works of Heinrich Hertz and Nikola Tesla, near the beginning of the 20th century, described in [2]. The first IEEE discussion on microwave power transmission took place in 1964 at the Clearwater, Florida conference on Energy Sources. While discussions have typically focused on intentionally directed power intended for reception by receivers designed for the task, the same principles apply for the reception of signal energy at arbitrary power levels and frequencies.

Beyond early applications involving wirelessly powering flying vehicles from the ground [2], researchers continued to design more efficient rectification circuits and antennas, leading to seemingly limitless combinations of different elements. As circuit sizes dropped, designers then began exploring means of collecting RF energy that was already available in the space around them, without the necessity for a dedicated power source installation.

There has been significant growth in this field over the last decade, due to the lowered power requirements in several common application circuits. Many incremental improvements have been brought forward in academic papers and conferences, as will be shown in the following pages. Furthermore, a handful of commercial product introductions have surfaced, aiming to bring RF energy harvesting or power transfer to the masses. Some of the pioneering companies behind these introductions include Powercast Corporation[5],

[5] (n.a.) Powercast. *Powerharvester Receivers.* Retrieved April 2012 from http://www.powercastco.com/PDF/Powerharvester-Brochure.pdf

AnSem[6] and MicroChip[7]. As of early 2012, there are mostly only development kits available and we have yet to see a direct consumer-oriented offering.

RF energy-harvesting technology is still progressing, which may explain the lack of solutions available to consumers at the time of this work's authoring. Reviewing recent literature on the subject, one might classify the incremental improvements into five major areas: novel antennas (such as those seen in [1], [4]-[13]), power combining from multiple sources (as shown in [6],[8],[9],[14] and [15]), impedance matching (see [4], [6], [8], [9]and [14]-[17]), different rectifying circuits (as included in [1], [4], [6]-[10] and [14]- [21]) and circuit miniaturization (as demonstrated in [14], [17], [20], [22], and [24]).

2.2.1 – Antennas Used in Recent RF Energy Harvesting Papers

The antenna innovations in the aforementioned works involve explorations of new antenna variations, including, but not limited to, rectangular antennas [11] (and arrays thereof), slotted patch antennas ([6], [7] and [12]), gap-coupled microstrip antennas [3], circular patch antennas [5], folded dipoles [13], circularly-polarized spiral antennas ([5] and [8]), planar inverted-F antennas (PIFA) [27] and fractal (particularly Koch) monopole, dipole and patch antennas ([9] and [32]).

When considering the implementation in this work, the key characteristics of an ideal antenna include an omnidirectional radiation pattern, a small physical antenna size, a feeding point that can easily be attached to the rest of the harvester circuitry, good multiband performance and high efficiency, all while remaining simple to produce consistently for various frequency bands, as they are found in different geographic locations. With this in mind, a printed antenna design will be selected (rather than traditional wire loops or helical

---

6 (n.a.) AnSem. *Expertise > Ultra low power.* Retrieved April 2012 from http://www.ansem.com/18/26/ultra-low-power

7 (n.a.) Microchip Technology Inc. *RF Energy Harvesting Development Solution featuring PIC MCUs with nanoWatt XLP Technology.* Retrieved April 2012 from http://www.microchip.com/stellent/idcplg?IdcService=SS_GET_PAGE&nodeId=2042&param=en551270

antennas) in order to allow use in standard electronic consumer device manufacturing. This method also reduces irregularity sources that can plague a more procedurally complex production run. This assumes a relatively uniform board stack-up with an equally uniform dielectric constant.

Rectangular microstrip patch antennas have been in wide use for many decades. The resonant frequency for the patch is controlled by its electrical length (L), while its impedance is controlled by the width (W)[42]. A commonly used design is the square patch shown in Figure 1, where $W = L = \lambda/2$.

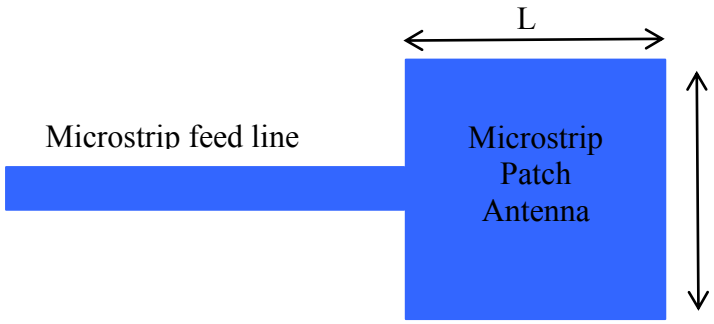

Figure 1 - Square Microstrip Patch Antenna

The microstrip feed line is also commonly inset into the patch, allowing some control of input impedance to the antenna.

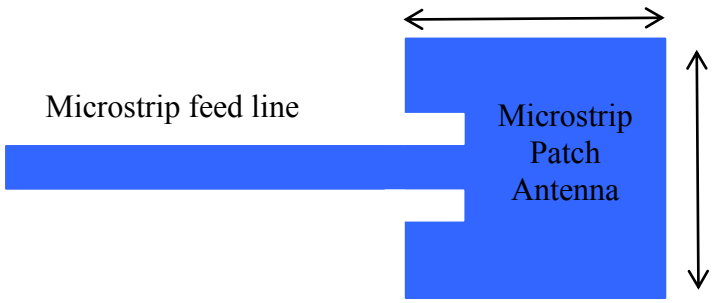

Figure 2 - Microstrip Patch Antenna with Inset Feed

Standard rectangular patch antennas are nevertheless inherently directional, exhibiting heightened gain in the broadside direction (or perpendicular to the patch surface) [23]. Rectangular patch antennas are also often combined in arrays (though not typically in energy harvesting applications), generally to aid in antenna directivity and further increase gain. The high directivity of any of these rectangular patch solutions causes varying performance based on the antenna's orientation, which makes it inappropriate for use in handheld consumer devices, as orientation is unpredictable.

Alternate options with more desirable radiation patterns are available by employing other microstrip geometries. We are however presented with a dizzying array of potential choices, as current manufacturing techniques allow virtually limitless custom copper designs, with tolerances in the range of $2/1000^{th}$ to $3/1000^{th}$ of an inch[8] (or 0.05mm).

Adding slots to coplanar patch antennas offers another alternative antenna configuration. This offers two distinct advantages over a standard rectangular patch antenna: potential size reduction and simplification of different polarization inclusions. More specifically, it is shown in [7] that a cross-shaped slot through the radiating patch permits a 32.5% reduction in patch size. The author apologizes for the crowded nature of Figure 3, however this was the only image of the antenna provided in [7]. Further, by using two orthogonal coupling slots, both linear polarizations are addressed. This increased the applicability of the antenna to different incoming polarizations. The antenna was designed for an energy harvesting application at 2.45GHz.

[8] (n.a.) Dynamic & Proto Circuits Inc. *Capabilities.* Retrieved May 2012 from http://www.dapc.com/dapc-capabilities/DAPCcapabilitiesbrochure.pdf

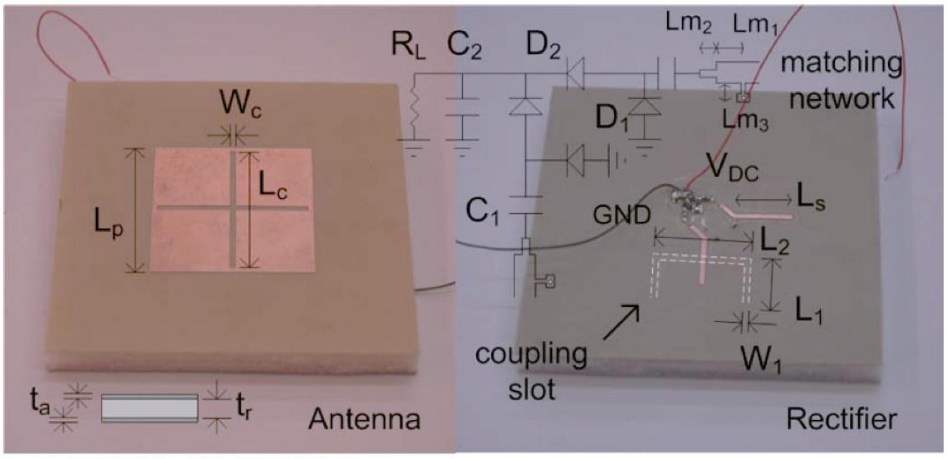

Figure 3 - Cross-Shaped Slot-Coupled Rectenna [7]

Another more complex example of this approach is presented in [6], where a multi-layer rectenna is designed using concentric annular rings (and a central circular patch), a slotted ground plane and an integrated phase shifter/rectifier, all shown in Figure 4:

Figure 4 - Slot-Coupled Multi-resonator (Triband) [6]

Each of the resonators targets a separate frequency band, with the 900MHz, 1760MHz and 2450 MHz bands being covered by the final design. The orthogonal slots in the ground plane, as in the last discussed design, ensure acceptance of additional signal polarizations. The phase-shifter permits coherent signal combination for increased charge collection.

Controlled metal spacing is also used in another fashion: parasitic gap-coupled antenna elements [3]. In this scenario, a center patch is the only radiating element fed and two parasitic patches of differing dimensions are positions near the main element in the same plane (see Figure 5).

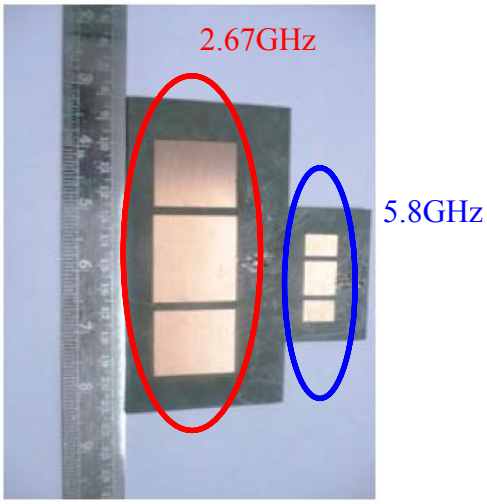

Figure 5 - Two Gap-Coupled Microstrip Antennas [3]

The major advantage in this case is an increase in gain and thus an increase in harvested power level, if the orientation of the receiving antenna with respect to the energy can be maintained. Again, this would limit personal consumer device or wireless sensor applications for which orientation cannot always be guaranteed.

Analogous to rectangular patch antennas, circular patch antennas cover a surface area dictated by the guide wavelength(s) of interested. The resonant frequency of a circular patch antenna is given in [25] as:

Equation 1:

$$f_{r,nm} = \frac{\alpha_{nm} c}{2\pi a_{eff}\sqrt{\varepsilon_{r,eff}}}$$

In Equation 1, the numerator is the mth zero of the derivative of the Bessel function of order m multiplied (for TM_{11}, α_{11}=1.841) by the free space velocity of light (c=3x10^8 m/s). The denominator is dependant on the effective radius (a_{eff}) and dielectric constant (ε_{eff}). For TM_{11}, with a target frequency of 2.4GHz, the radius on standard 25mil FR4 substrate, the target radius of the circular patch would be:

Equation 2:
$$a_{eff} = \frac{\alpha_{nm} c}{2\pi f_{r,nm}\sqrt{\varepsilon_{r,eff}}} = 19.0mm$$

As can be seen from Equation 1 and Equation 2, the standard circular patch is designed for a single operating frequency at a time. This would not allow the targeting of multiple, which is a major requirement in our case. The radiation pattern, shown in Figure 6, is principally directional in the broadside direction, which remains non-ideal for our application.

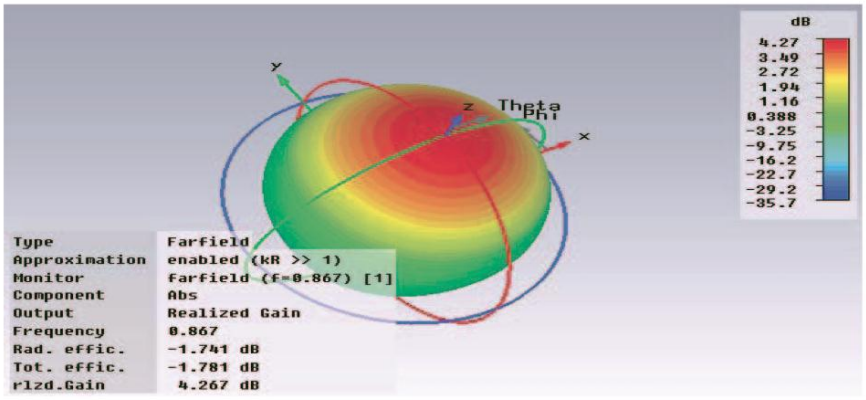

Figure 6 - Radiation for Center-Fed Circular Patch [26]

Next, we take a look at folded dipoles, which have been implemented in both free space [13] and printed microstrip [1] forms. In the free space (non-printed) version, the author of [13] fabricated a soldered folded dipole attached directly to a standard SMA connector for his energy-harvesting application. Though this implementation showed a roughly 4% increase in rectification efficiency (to 15.43%) over an equivalent loop antenna,

the implementation is susceptible to physical damage, as it is not supported by a substrate or other stabilizing structure. Details on size were not expressly given, though the photo in Figure 7, with the antenna next to a 1€ piece (which has a 23.25mm diameter) gives us a means to approximate the size of the antenna at 25mm x 55mm=1375mm^2. The return loss is narrowband and contains only a -3dB return loss minimum at the center target frequency of 300MHz. Nonetheless, the expected toroidal radiation pattern for a dipole should provide a good omnidirectional characteristic for a power harvesting application.

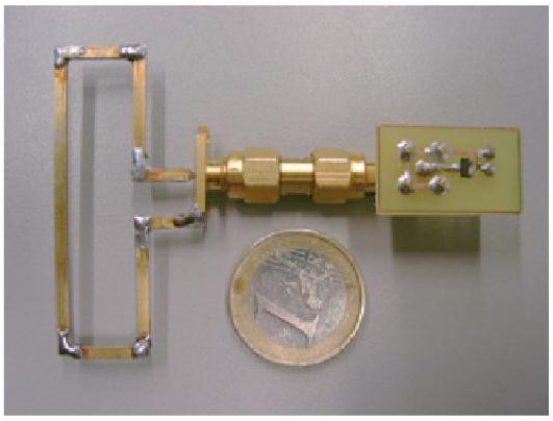

Figure 7 - Folded-Dipole Implementation at 300MHz [13]

Another type of printed antenna that has seen increasing study in recent years is the spiral antenna (see Figure 8). An earlier implementation of an antenna array to be used for wireless powering of industrial sensors was introduced by Hagerty et al. [8]. In that implementation, a 64-element array of printed spiral antennas (shown in Figure 9) was constructed using series and parallel connections of array elements to achieve acceptance of both left-hand circularly polarized (LHCP) and right-hand circularly polarized (RHCP) signals. The authors also experimented with different DC combinations of the different rectifier outputs. The best rectification efficiency (20%) achieved was when all 4-element sub-arrays were all connected in parallel. The total implementation was contained within a frame of 18.5 x 18.5cm (34225mm^2). Relatively stable performance across 2-8GHz was obtained, with test input power levels of -15.5dBm, -7.5dBm and 17.3dBm. Due to the

orthogonal configuration of neighbouring antenna elements, the author did produce a flat polarization response, at the expense of an average loss of 3-dB for every possible polarization of the incident energy,

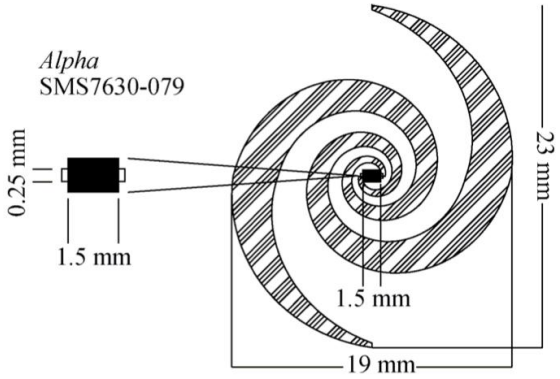

Figure 8 - Single Spiral Antenna Element [8]

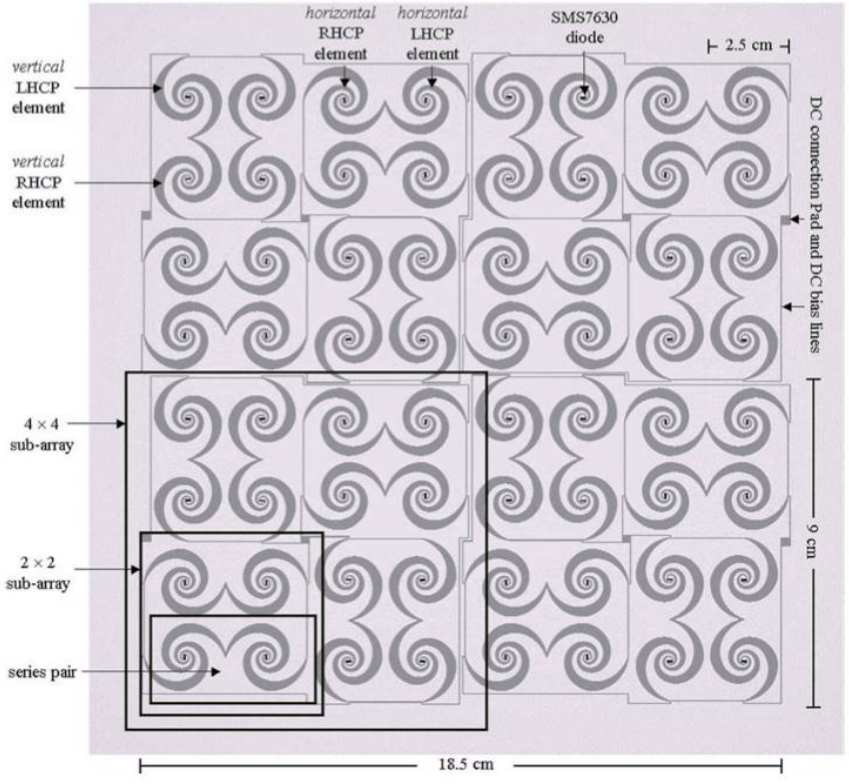

Figure 9 - Array of 64 Spiral Antenna Elements[8]

Another recent implementation of a single spiral antenna can be found in [5]. In this implementation, wideband frequency response was also shown (with minimum -10dB return loss simulated from 1.6GHz to 4.0GHz). Radiation patterns for the single element were also provided and varied with frequency, but did not produce sharp gain peaks, which would be non-ideal for our implementation.

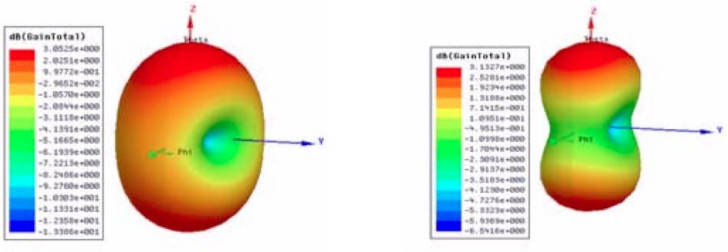

Figure 10 - Spiral Antenna Radiation Patterns at 1.85GHz(a) and 2.45GHz(b) [5]

The size of a spiral antenna is predominantly determined by its lower operating frequency, as its outer radius, R, is related to this frequency by the following equation[8]:

Equation 3

$$R = \frac{c}{2\pi f_{low}}$$

Planar inverted-F antennas (PIFA) are also seeing widespread used on cellular handsets and other cellular and ISM band applications. A PIFA is in essence a raised patch antenna, shorted to the ground plane at one end (either by a pin or any width of perpendicular conductor) and fed through another pin or via at a pre-determined location in the patch, based on target frequency. An example of one such antenna in an energy-harvesting application can be found in [27], which targets the 2.45GHz band. In this example, illustrated in Figure 11, uses a full-width grounding wall (W_a = 12mm) and contactless feeding mechanism via a feed line on the underside of the board and an aperture in the ground plane. This particular implementation was relatively narrowband, with 10dB return

loss being obtained across approximately 25MHz, centered at 2.45GHz. Sizing of the design was not optimized, with total dimensions of (90x40x2)cm^3.

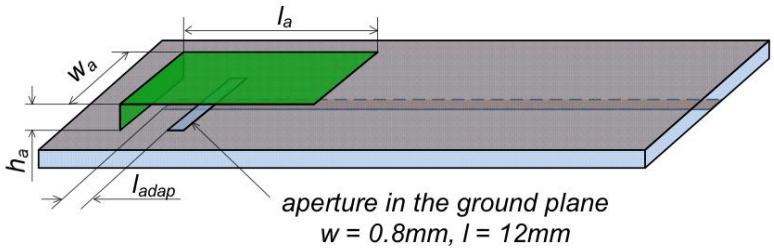

Figure 11 - 2.45GHZ PIFA Antenna Proposed in [27]

As described in [42], maximum relative bandwidth can be approached with the PIFA when either of the following conditions are true: (i) the width of the shorting tab is equal to the width of the raised patch (as is the case in Figure 11) and (ii) the length of the patch is at least 2 times the width of the patch. When the first condition is true, the length of the raised plane should be λ/4. In either case, the maximal relative bandwidth noted is 10%. To achieve multiband behaviour, one can either nest multiple PIFA's within a physical space or create L- or U-shaped slots in the plate to create additional operational bands[42].

Evidently, construction of PIFA is more complex than a printed antenna and is susceptible to both physical variations in assembly and physical damage due to the potential fragility of both the grounding and feed point connections.

Particular attention has been drawn to fractal antennas in recent years, as they see increasing use in modern designs. In essence, these methods employ an iterative transformation effected on the segments of some simple starting shape. Figures 1 to 3 show examples of some common planar patch antennas based on fractal geometries.

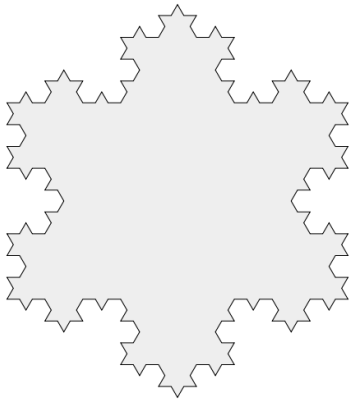

Figure 12 - 'Koch Snowflake', 3rd Iteration[9]

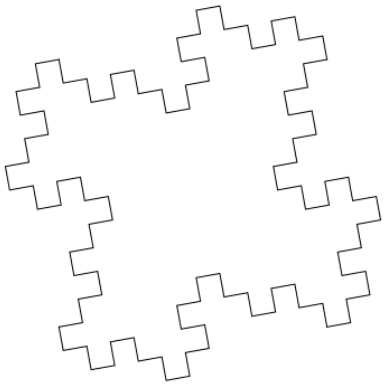

Figure 13 - 'Minkowski Sausage', 3rd Iteration[10]

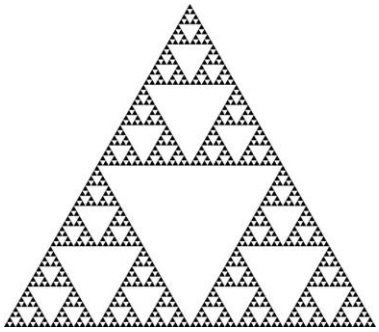

Figure 14 - Sierpinski's Gasket, 6th Iteration[11]

[9] WikiMedia Commons. *Koch Snowflake 3rd Iteration.SVG.* Retrieved May 2012 from https://commons.wikimedia.org/wiki/File:Koch_Snowflake_3rd_iteration.svg

[10] Wolfram Alpha. *Minkowski Sausage – 3 Iterations.* Retrieved from http://www.wolframalpha.com/entities/calculators/minkowski_sausage/pk/py/ew/

[11] Wilde, S. *(untitled)* Retrieved May 2012 from http://www.stuartwildeblog.com/visionaries/?currentPage=2

These interesting geometrical adaptations offer more efficient use of space, within the confines of a given PCB outline. Being able to fit more metal into a given space allows the designer to create more electrical length, thereby achieving lower operating frequencies. This, along with increasingly broadband impedance matching [28] and methodically simple implementation make fractal antennas key candidates for integration into RF energy harvesting circuits.

This concept can also be extended to include meandered line monopole or dipole antennas. In this case, we effect the transformations on an open- or closed-ended microstrip stub and, as first approximation, maintain a generally omnidirectional radiation pattern. The next few paragraphs detail two of the most popular such implementations: the Minkowski fractal and the Koch fractal.

The Minkowski transformation is defined in at least three different ways in the available literature (see [29]-[31]). For the sake of brevity, only the most popular implementations will be discussed here. It has also been referred to as the quadratic Koch Curve. In this description, the starting segment becomes 8 sub-segments, all of which measure ¼ of the original segment's length (*L*). See Figure 15 for a visual representation of the transformation.

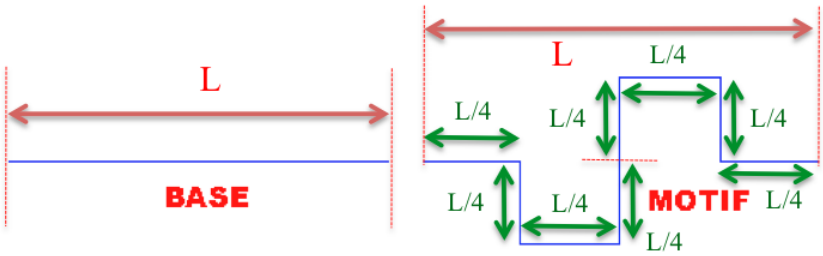

Figure 15 - Minkowski Sausage Transformation[12]

[12] Image modified from: ThinkQuest. *Minkowski Sausage.* Retrieved May 2012 from http://library.thinkquest.org/26242/full/fm/fm24.html

The result is a total segment length of 8 x (L/4) = 2L, where L is the original segment length. This is accomplished without passing the boundaries of the start and end points of the original figure. As this process is repeated on each of the newly formed segments, we see the progression as shown in Figure 16. This has obvious benefits when attempting to fit a given length of microstrip (such as a λ/4 monopole) into a restrictive space. Unfortunately, as a consequence, there are progressively more coupling interactions between segments as they become closer to one another. This must therefore be included in any simulation model. Further to this, there is a significant increase in the perpendicular direction (2 x L/4). This is one area where the Koch fractal holds an advantage.

Three subsequent iterations of the transformation are shown in Figure 16, depicting the increase in overall line length and the space-filling nature of the algorithm.

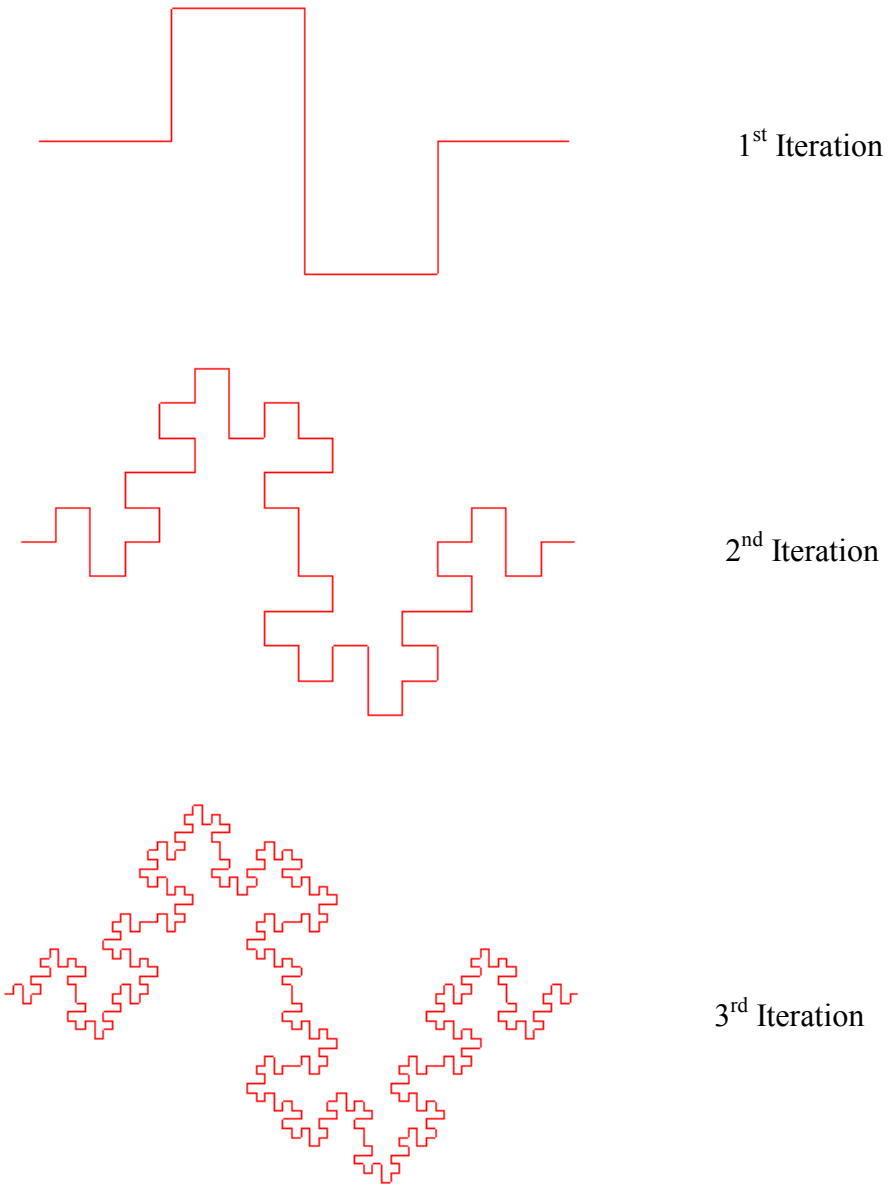

Figure 16 - Minkowski Sausage Iterations[13]

[13] MathCurve. *Saucisse de Minkowski.* Retrieved May 2012 from http://www.mathcurve.com/fractals/minkowski/minkowski.shtml

The Koch transformation is obtained by dividing a segment into three equivalent lengths, before replacing the middle segment with two sub-segments of the same length, which then form a peak above the original segment's axis. These new sub-segments form an equilateral triangle with the length of segment that they have replaced. This necessitates angles of 60° from the original axis. The process is visually shown in Figure 17.

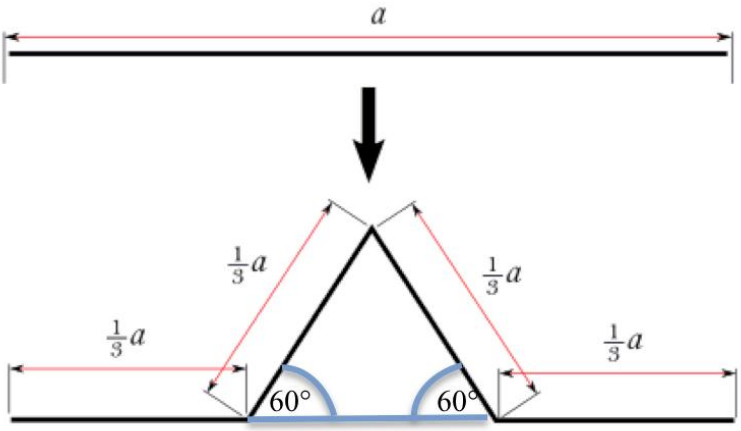

Figure 17 - Koch Transformation Process[14]

As the process is repeated on all newly obtained sub-segments, one can see the obvious increase in total line length within a given area. An iteration produces a 4/3*L* line length increase and only increases the perpendicular dimension by 1/3*L* sin 60° ≈ 0.29*L*. The results of three iterations are shown in Figure 18.

[14] Modified from Wordpress. *The Koch Snowflake.* Retrieved May 2012 from http://dorchard.wordpress.com/2009/02/18/the-koch-snowflake/

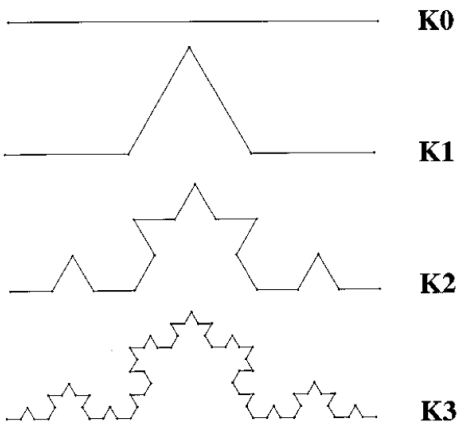

Figure 18 - Results of Three Subsequent Koch Transformation on a Line Segment

As both the start and endpoints remain stationary, the transformation can easily be applied to all sides of an arbitrary polygon.

The authors of [28] developed a rigorous transformation relationship to describe the Koch iterations mathematically. These are included for completeness. If the starting vector is described by two endpoint coordinates, x_1 and x_2, then an affine transformation can by described as:

Equation 4

$$\omega_n \begin{pmatrix} x_1 \\ x_2 \end{pmatrix} = \begin{pmatrix} a & b \\ c & d \end{pmatrix} \begin{pmatrix} x_1 \\ x_2 \end{pmatrix} + \begin{pmatrix} 0 \\ 0 \end{pmatrix}$$

where there are four new bi-coordinate endpoints described by:

Equation 5

$$\omega_1 \begin{pmatrix} x_1 \\ x_2 \end{pmatrix} = \begin{pmatrix} 1/3 & 0 \\ 0 & 1/3 \end{pmatrix} \begin{pmatrix} x_1 \\ x_2 \end{pmatrix} + \begin{pmatrix} 0 \\ 0 \end{pmatrix}$$

$$\omega_2 \begin{pmatrix} x_1 \\ x_2 \end{pmatrix} = \begin{pmatrix} 1/3\, cos60 & -1/3\, sin60 \\ 1/3\, cos60 & 1/3\, cos60 \end{pmatrix} \begin{pmatrix} x_1 \\ x_2 \end{pmatrix} + \begin{pmatrix} 1/3 \\ 0 \end{pmatrix}$$

$$\omega_3 \begin{pmatrix} x_1 \\ x_2 \end{pmatrix} = \begin{pmatrix} 1/3\, cos60 & 1/3\, sin60 \\ -1/3\, sin60 & 1/3\, cos60 \end{pmatrix} \begin{pmatrix} x_1 \\ x_2 \end{pmatrix} + \begin{pmatrix} 1/2 \\ 1/2\sqrt{3} \end{pmatrix}$$

$$\omega_4 \begin{pmatrix} x_1 \\ x_2 \end{pmatrix} = \begin{pmatrix} 1/3 & 0 \\ 0 & 1/3 \end{pmatrix} \begin{pmatrix} x_1 \\ x_2 \end{pmatrix} + \begin{pmatrix} 2/3 \\ 0 \end{pmatrix}$$

Variations on the Koch are numerous in the literature (including [28], [32]). One variation in particular [32] explores a mirrored combination of a meandered printed dipole joined with an end-loaded dipole employing Koch loops. The size of the antenna is further modified via the addition of concentric, but unconnected (gap-coupled) Koch loops inside the connected loops (Figure 19).

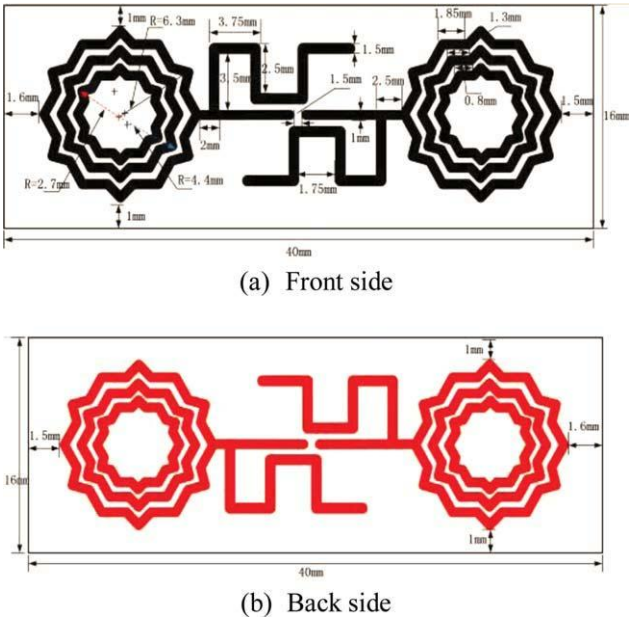

Figure 19 - Tri-Band Antenna, End-Loaded with Koch Fractal Loops (From [32])

As claimed in [32], the first interesting result was a 35% decrease in overall size of the printed circuit. This was while still maintaining the same FR4 material, with a dielectric constant ε_r=3.7 and a material thickness of 1.5mm (or just under 60mil). The second

interesting result was a more omni-directional shape for the E pattern, which properly suits an RF energy harvesting implementation aimed for consumer use.

Claims of unique multiband properties of fractal antennas have been questioned in recent works by S. Best ([33],[34]). In [33], it is shown that a Hilbert-curve fractal monopole offers no remarkable advantage over a meander line monopole of same overall length. These measurements were done up to a maximum frequency of 300MHz. The author of [33] does however mention that that as operating frequency increases (and thus antenna size becomes larger with respect to wavelength), antenna geometry becomes a more important factor in determining the antenna's multiband behaviour. There are benefits to the space-filling nature of the Hilbert fractal, but with increasing iterations, a decrease in bandwidth and efficiency are observed [33]. For the more common Koch fractal, the author of [34] indicates that certain self-similarity elements of the iteration do have a significant (though not completely unique) effect on the multiband behaviour, especially in the higher tested bands (up to 6GHz). There is thus still merit in pursuing the use of this type of antenna. It offers good multiband performance, with a high level of trace compression, resulting in small physical size. Though the self-similar geometry does not offer unique benefits, it does offer a simple, repeatable means of obtaining these benefits. In fact, for the meandered antennas in [34] modified to match the Koch performance, all three antennas (M3, M4 and M5) are said to owe their behaviour in large part to their outline, which is in fact a first-order Koch fractal transformation of a straight monopole (see Figure 20).

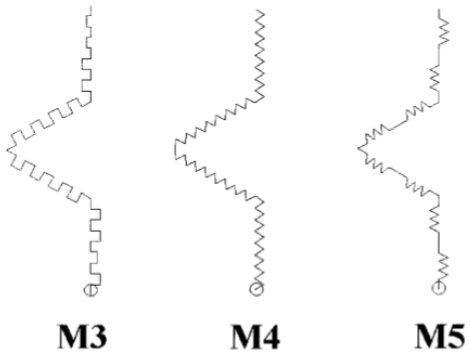

Figure 20 - Meander Line Antennas from [34]

2.2.2 – Power Combining

Power combining has been demonstrated in several ways in the literature, including RF combining of the received power from multiple antennas. The end goal is always to increase the amount of harvested RF energy. This has been attempted by implementing several antennas at the same frequency [15], where four identical meandered monopoles were printed in the same area, each offset by 90° (Figure 21). The result, as can be expected, was a significant increase in output power available from the antennas when compared to a single meandered dipole. The author of [15] describes a measured 284% in operational range (or theoretical 300% increase in power available from the antennas), at the expense of an 83% increase in area occupied by the antennas.

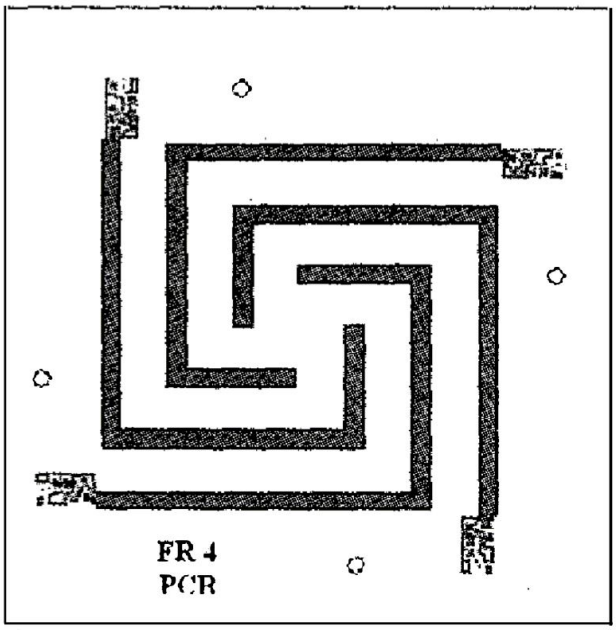

Figure 21 - Multiple Antennas in Same Space [15]

The author of [32] demonstrated a different configuration by grouping antennas tuned to a handful of targeted frequencies, though not in an energy-harvesting application. The configuration combined Koch fractal loops at 915MHz with meandered structures aimed at the 2.45GHz band (see Figure 19). The benefits for tapping multiple operational frequency

bands are evident, as additional energy sources become viable (in this case, cellular and WiFi network transmitters).

Attempts were also made to combine several pre-rectified signals (DC-combining, as seen in [9]). A direct comparison between the RF-combining topology and the DC-combining topology is actually presented in [9]. It is shown in [9] that combining at the RF level allows more optimum power harvesting near the main receiving lobe, when speaking of directional antennas. Nonetheless, once the angle of reception is deviated more than +/- 25º from the main lobe, the DC-combining proves to offer slightly superior performance.

2.2.3 – Impedance Matching

Impedance matching is another challenging concern, which stems primarily from the inconsistent impedance of the nonlinear rectifying elements (whether considering diodes or transistors). As varying potential is applied to the junction, junction capacitance changes slightly. Thus the impedance varies with the amount of input power presented to it. Consequently, any static matching network is only truly effective over a finite input power range. This problem is clearly magnified when there are multiple antennas and/or multiple rectifiers. A means of addressing this issue, resistor emulation, is presented in [4] and [36] and us further discussed in Section 2.2.4.

A more radical design is shown in [35], where varactors are employed, along with a feedback signal proportional to the load current in order to dynamically modify the matching network to suit the current operating conditions. An increase of 100-150% in rectifier efficiency was noted through simulation. Calibration of the feedback is nonetheless required prior to deployment.

2.2.4 – Rectification

Several attempts to enhance the efficiency of diode rectification have also been made in the literature. The use of PMOS transistors to replace diode-connected NMOS transistors

as rectifying elements allows a reduction in threshold voltage and a 5% relative increase in rectifier efficiency [17]. This is an interesting option for CMOS implementations (but outside the scope of this work).

The idea of resistor emulation for the purpose of tracking the peak power point over a wide range of incident power levels is explored in [4] and [36]. This effectively increases the optimal input power range over which the rectifier remains efficient. Since the implementation at hand does not enjoy the luxury of predetermined input power levels, such a circuit improvement could prove quite valuable in future work.

Several papers have also proposed the notion of sacrificial biasing ([16], [17], [20]), a technique where DC bias is applied to the rectifying element's input in order to reduce the required threshold voltage needed to allow conduction. At the expense of some output current, the circuit's efficiency was shown to increase by 60% over the non-sacrificial equivalent NMOS circuit [17].

Many topology adjustments to the standard Greinacher and Dickson rectifiers have been proposed and tested in the literature, with varying levels of success. Villard voltage multipliers are commonly employed in rectification circuits that expect low input voltages during operation. Figure 22 depicts an example of a single stage Villard voltage multiplier (a doubler in this case), in which each stage consists of two capacitors and two diodes. As AC voltage is applied at the input, (which would embody the RF voltage received by the antenna in our case), the opposing orientations of subsequent diode elements ensure that voltages are added as the alternating current changes directions. Each such stage doubles the input voltage.

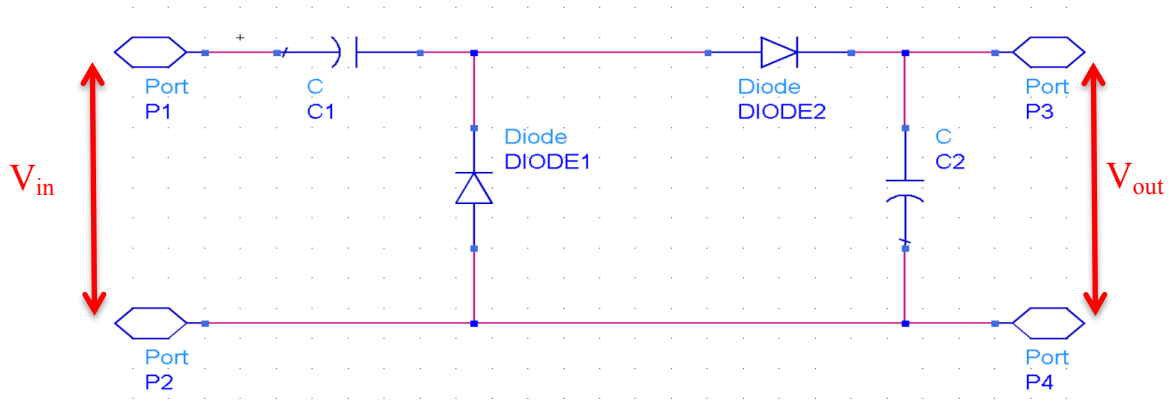

Figure 22 - Single Stage Villard Voltage Multiplier

Assuming an AC input, we should see voltage as follows: During the negative half-cycle, C_1 will be charged through *Diode 1* (the relative potential will be V_{in}). During the positive half-cycle, the input voltage, V_{in} will be added to the built-up potential in C_1 to create a doubled potential of 2 x V_{in} across the terminals of C_2, after passing through *Diode 2*.

V_{out} will theoretically achieve twice the voltage at the circuit's input, *once the circuit has reached steady state*. These stages could, in an ideal case, be cascaded N times in order to produce a theoretical output of V_{out} = 2N x V_{in}. There are, however, limitations to the efficiency of such a circuit, including non-negligible reverse leakage currents and forward series resistance in each of the diodes, as well as voltage losses in the coupling capacitors and diode junctions. We can visualize the notion of stage cascading in Figure 23, as we introduce the next topology, the Greinacher rectifier.

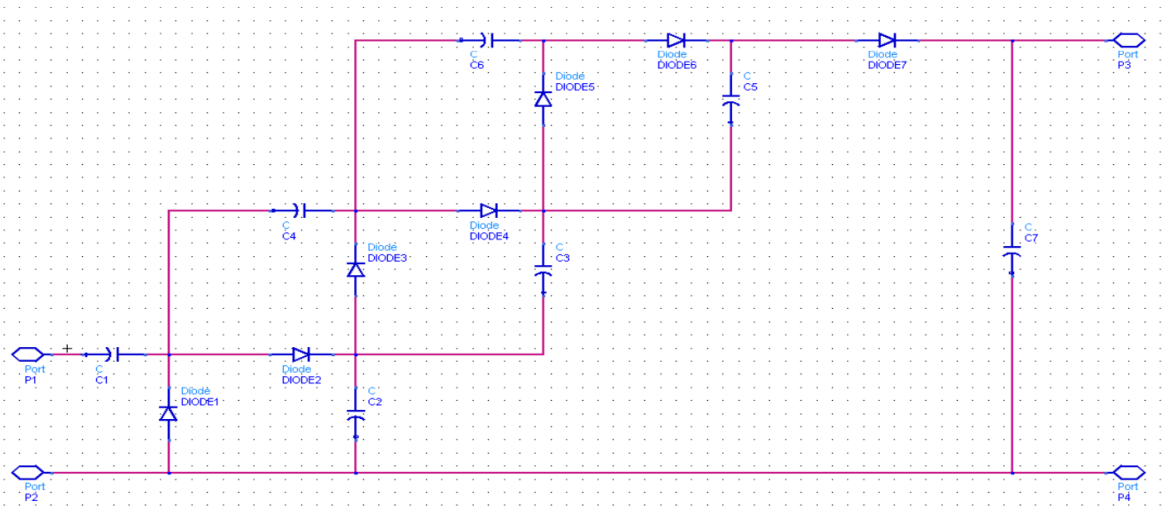

Figure 23 - Three-Stage Greinacher Rectifier

The Greinacher configuration (also known as Cockcroft-Walton) is essentially a Villard multiplier, with the addition of a peak-detector rectification stage at the output. Figure 23 contains a three-stage version of this topology, which results in a theoretical 6:1 ratio of V_{out} to V_{in}. It has been shown in [19] that the optimal trade-off between voltage gain and the limitations imposed on voltage ripple and output current is a 'six stage' multiplier. In this case, the author of [19] is referring to six *active elements*, not six full (4-element) groupings. This corresponds to Figure 23, without the output peak detector rectification stage.

The Dickson multiplier, another topology often mentioned in the literature, is an adaptation of the Greinacher configuration, with the distinction of requiring a DC input signal for operation. Due to the AC nature of our target signals, this topology has been eliminated from consideration for this design.

In the different types of multipliers/rectifiers mentioned above, Schottky diodes are primarily selected for discrete components designs. This is principally owed to their low turn-on voltage (0.3-0.5V, compared to 0.6-0.8V for a silicon *pn*-juction diode [37]), which minimizes junction voltage losses through the stages of the voltage multiplier. These diodes

also exhibit fast switching speed, which allows use in high frequency applications.

2.2.5 – Rectenna Design Approach

Many papers (including [6]-[8]) have also explored the joint design of antenna and rectifier as one complete entity, commonly referred to as a 'rectenna'. This integrated design method aims to reduce the size of the final design, as well as streamline the design process, by eliminating unnecessary intermediate steps. For example, [8] shows the use of a source pull simulation on the rectifying diode, utilizing harmonic balance to determine the optimal source impedance that the antenna should present to the diode over a range of expected input power levels. These results will allow the antenna designer to use this as a design goal while designing the antenna, eliminating the need for a separate matching network. This method will be employed in this work, though a multi-stage Greinacher rectifier, rather than a single diode, will be source-pulled.

2.2.6 – Miniaturization

Beyond the scope of this work are other important advancements, such as the design of energy storage elements that are more suitable for the small charge collection seen in RF harvesting applications, as well as the invention of new energy management techniques for more efficient storage [36]. Further, there is the continuing miniaturization of harvesting circuits using various CMOS processes (examples of which are found in [20] and [22]). These interesting topics will likely be the focus of many papers to come, as they will enable the ushering of RF energy harvesting into smaller mainstream consumer goods. Improvements in efficiency were brought forth by using minor modifications, such as substituting out the typically used diode-connected NMOS transistors for PMOS versions [17], thereby reducing the net threshold voltage for the junction. Nonetheless, in aiming to simplify rapid prototyping iterations, it was decided to limit circuit topologies to those that could be easily constructed using only cost-effective small run PCB manufacturing techniques, using microstrip lines and readily available discrete components.

2.3 – Comparison of Selected Works

Table 1, summarizes the results of several recent works relevant to the one presented in this thesis. It shows that most efforts have occurred at 2.4GHz, likely due to the widespread worldwide use of this frequency range. RF to DC efficiency results have ranged between 6.5 and 30%. Although many designs have employed large antenna arrays, some efforts have occupied as little as $4cm^2$ of area.

2.4 – Conclusion

In this chapter, an overview of the recent history of energy harvesting and a state of the art literature review of some important papers that are relevant to the harvesting of ambient RF energy have been presented. The rectenna configuration, based on PCB technology and readily available discrete components has been retained as the most appropriate in this work. In the next chapter, the design of such configuration will be investigated

Table 1 - Comparison of Demonstrated Performance in Selected Works

Reference	Topology	RF to DC Efficiency	Operating level	Operating Frequencies	Physical Dimensions
[5] Simulation	Spiral antenna, four-element voltage doubler	**13%** P_{DC}=1.3 μW from P_{RFin}=-20 dBm	**< 1V** R_L=7.4kΩ @ P_r=-20dBm	**2.4GHz**	*(not indicated)*
[7] Measurement	Dual-polarized, aperture-coupled patch antenna, voltage doublers	**15%** P_{RFin} = 0.15 μW/cm^2 on 79.7 cm^2 aperture P_{RFin} = -19.2dBm	**90mV** R_L=4.5kΩ @ P_r=-19dBm	**2.44GHz**	≈ 6cm x 6cm
[9] Measurement	2x2 Koch antenna array, modified Greinacher rectifier	**30% (*)** P_{DC} = 3μW from P_{RFin}=-20 dBm	*(not indicated)*	**2.45GHz**	Less than 2cm x 2cm, plus rectifier
[11] Measurement	Patch antenna, microstrip matching and LPF, DC/DC converter	**21%** P_r=-10dBm, R_L= 1.3kΩ	**1.5V** R_L=1.3kΩ @ P_r=-10dBm	**2.45GHz**	5cm x 6.5cm (plus DC-DC converter)
[13] Measurement	Folded dipole antenna, single Schottky diode	**15.43%** P_{DC} = 213μW from P_{RFin}=+20 dBm	**2V** R_L=3kΩ @ P_r=+20dBm	**300MHz**	≈ 5.5cm x 10cm
[16] Measurement	Villard voltage doubler, switched capacitor DC/DC converter	**6.5%** P_{DC}=162nW from P_{RFin}=2.5μW	**1V** R_L=5MΩ @ P_r=-25.5dBm	**2.2GHz**	Not detailed, though **CMOS** with 120nm/130nm process
[36] Measurement	Resistor emulation, rectangular patch and spiral rectenna array	**23.8%** P_{DC}=600μW from P_{RFin}=70μW/cm^2 on 36cm^2 aperture	**4.15V** R_L=1kΩ @ P_r=-25.5dBm	**2.4GHz**	6cm x 6cm

(*) efficiency defined as ratio of DC power output to power at input of rectifier

Chapter 3 – Design Considerations

In this chapter, design considerations for the energy harvester design, as well as the selection of individual component topologies will be outlined. Based on references presented in Chapter 2, choices are made for the multi-band antenna and voltage multiplier/rectifier. These will form the basis of the design.

3.1 – Ambient RF Energy Sources

Up until this point, we have kept the discussion to very general terms, thereby giving an overview of previous attempts at RF energy harvesting and theories on what improvements can be achieved. The bands targeted for harvesting in this thesis will be those that are the most readily available to the general Canadian population. These include Wi-Fi hotspots (and other 2.4GHz sources, as listed in Section 1.2), as well as cellular (850MHz band) and Personal Communications Services (1900MHz band) network transmitters.

The proliferation of Wi-Fi functionality across just about every commercial wireless device has driven a steady creep of Wi-Fi hotspot coverage across most urban and suburban areas, as well as many rural areas. Typical maximum transmit powers for a Wi-Fi hotspot fall in the order of +10 to +20dBm, or 10 to 100mW. Of course, depending on one's proximity to the source, the effective received power can be much less.

Cellular and PCS coverage, for their part, have also greatly expanded throughout much of the country's geography. Conversations about how many 'bars' one's phone is getting have become common occurrences. This method of displaying received power level, or Received Signal Strength Indicator (RSSI), is analogous to how much DC energy an RF energy-harvesting circuit will be able to provide, as this will directly depend on the received signal strength.

3.2 – Expected Power Levels

When considering any one of these power sources, one can simplistically estimate the approximate theoretical power available at any given distance from the emitter based on the Friis equation below:

Equation 6

$$P_r = \frac{(G_t G_r \lambda^2)}{(4\pi R)^2} P_t$$

The equation shows that the power decreases as the square of the distance (R) from the source grows. Also factored into the equation are the transmitted power (P_t) and the gain of both the transmitting (G_t) and receiving (G_r) antennas. It is thus clear to see that one would benefit from the ability to draw from the nearest power sources, regardless of frequency. This equation in no way accounts for multipath fading losses or changes in transmission media, such as objects between the radiator and receiver.

As mentioned in Section 2.1, a recent Dutch study revealed that the summed power density across the 935-960MHz band in Eindhoven, Holland, varied between 0.1mW/m^2 and 3.0mW/m^2 (and depended greatly on the amount of GSM traffic at the time of measurement). It was also shown that only operating mobile phones produced enough RF energy to power a small appliance via a rudimentary RF energy-harvesting circuit.

3.3 – Block Diagram of Implementation

The general functioning of the intended design is laid out in Figure 24. This configuration offers simple integration of the selected antenna, rectifier and storage element into a single PCB. By keeping the circuit to its most basic functional blocks, we eliminate any losses that could be incurred by additional filters, switches, etc. As discussed in Section 2.2.2, this configuration also provides superior power harvesting in the main lobe, when compared to a DC-combined configuration. Ambient radio frequency waves will be received by the tuned antenna array, whose elements are combined and fed to the rectifier section. The resulting DC charge is passed on to a charge storage element.

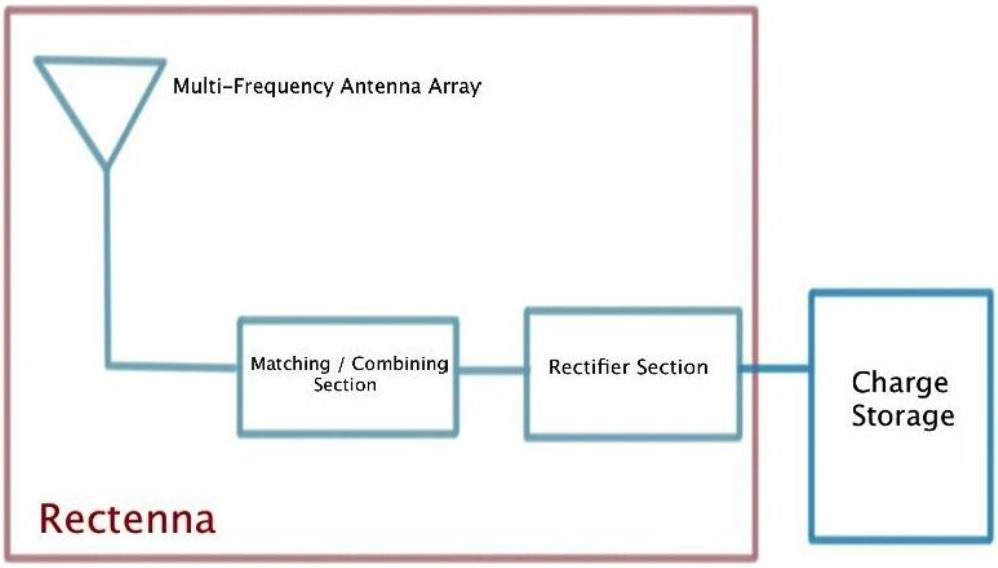

Figure 24 - High-Level Implementation Diagram

3.4 – Further bounding

Before any signal rectification or signal treatment can be done, we must first ensure that the energy arrives at the rectifying device with the highest power and least waste of energy via thermal effects or impedance mismatches. This means choosing an antenna solution that can accept the expected types of signal polarization and equally importantly, the targeted operational frequencies. A suitable pattern for radiation acceptance must also be

chosen.

Generally speaking, the use of a highly directional antenna, such a Yagi-Uda or parabolic design is impractical for consumer use, as it would require the user to actively seek out RF sources and re-orient the capture antenna accordingly. The use of a more omni-directional pattern, such as those theoretically offered by a monopole or dipole implementation would be an evidently more suitable answer, though they would not collect as much energy from a given fixed source, due to their lower gain.

Ideally, a circularly polarized antenna would seem to be the most efficient choice, since it will accept both vertically and horizontally-polarized signals. Many such designs are available and have been tested in practice [6], [8], [38].

The inclusion of multiple receive antennas, or a multi-frequency antenna, allows us to gain access to more energy sources and thus more average energy. A method implementing two antennas was demonstrated in [14], where antennas were deployed for both 400MHz and 2.4GHz. Another method, though using only one operating frequency, utilized several antennas for that frequency [15], creating polarization and spatial diversity. This increases the chance of receiving the maximum power available.

The methods used for signal rectification are numerous in their implementations and the choices were narrowed down to include only the most efficient types in Section 2.2.4. In [19], a three-stage (six active element) Villard voltage doubler circuit (VDC) was shown to be the optimal configuration. It uses Schottky diodes, thereby taking advantage of their high current delivery, fast transition speeds and low turn on voltage.

The following sections will describe the design considerations of a rectenna system targeting the 850MHz, 1900MHz and 2.4GHz bands. This will involve individual antennas tuned to each frequency band. These will then rectified and combined to supply a common energy storage element. The design of the antennas and matching sections will be based on the results of simulated source-pull for the selected rectifying diodes.

3.5 – Antenna Selection

In order to achieve maximal energy collection by targeting several highly used frequency bands, a multi-frequency antenna design with an omnidirectional radiation pattern will be targeted. Although a circular polarization would be ideal, it will not be used in this case, due the added implementation space required, and tight design sizing constraints. A summary of several current antenna designs used in recent energy-harvesting applications is provided in Section 2.2.1.

Table 2 aims to compare the aforementioned antenna topologies based on the discussion above. Here, physical size is described in relation to wavelength, multiband behaviour indicates the ability of the topology to cover more than one operational band at a time and bandwidth describes the frequency range covered around the central operating frequency. Qualitative descriptions are also for the theoretical radiation pattern, the difficulty level of fabrication, the ability to quickly scale the design for new operating frequencies and the level of difficulty relating to properly feeding/tapping the antenna.

Table 2 - Comparison of Antennas Discussed

	Electrical Size	Multiband Behaviour	Bandwidth	Radiation Pattern	Construction Difficulty	Scalability with Frequency	Level of Feeding Difficulty
Rectangular Patch	λ/2 x λ/2	Good (with modification)	Small	Directional (especially in array)	**Low**	**Easy for simple patch**	**Low**
Slot-Coupled Multi-Resonator	λ/2 x λ/2 (of lowest freq)	**Excellent**	Medium	Directional (broadside)	Med	Difficult	High
Gap-Coupled MS Patch	λ/2 x λ/2 Plus parasitic elements	Good (with modification)	Medium	Directional (broadside)	**Low**	Difficult	**Low**
Circular Patch	(Circle inside:) λ/2 x λ/2	Poor	Medium	Directional (broadside)	**Low**	**Easy for center feed**	Med
Folded Dipole	< λ/2 x λ/2	Poor	Small	**Toroidal**	**Low**	**Easy**	**Low**
Spiral	**λ/2π x λ/2π**	**Excellent**	**Excellent**	Directional (broadside)	Med	n/a	**Low**
PIFA	**λ/4 x <λ/4**	Good (with modification)	Good	**Semi-Toroidal**	High	Difficult	Med
Koch Fractal	**λ/4 x λ/8**	**Excellent**	Good	**Semi-Toroidal**	**Low**	**Easy**	**Low**

Table 2 shows that in order to meet tight sizing constraints and target multiple operational bands, the interesting choices are slot-coupled multi-resonators, printed spiral antennas, planar inverted 'F' antennas (PIFA) and a fractal implementation, such as the Koch. When simplicity of fabrication is considered, the PIFA and spiral antenna designs are more dependant on manufacturing tolerances. The spiral antenna is also quite directional, which does not fit the use we seek. The fractal loop implementation stands above the slot-coupled multi-resonator through its ability to be quickly and methodically re-scaled/re-fabricated for different frequency bands. By maintaining a repetitive segmentation process during meandering, the figure can be parameterized by the number of sides in the starting shape, and the length of a segment. This should allow rapid scaling to a new frequency band via a single parameter change

As a basis for the design, the topology proposed in [32] will be adapted to the energy-harvesting application that this work attempts to target. As such, adjustments to impedance, as seen by the voltage multiplier/rectifier circuit will need to be adjusted. The frequency response from the original design is shown in Figure 25.

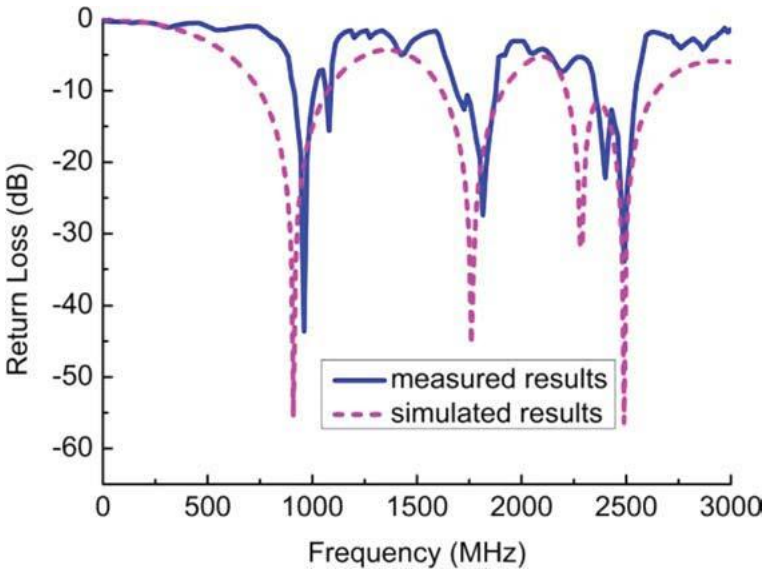

Figure 25 - Return Loss results for Zhou Antenna [32]

As can be seen in Figure 25, two frequency bands targeted in [32] are common to this

work (900MHz band and 2.4GHz band). These further reinforce the design as a good candidate for optimization in this work.

3.6 – Voltage Multiplier and Rectifier Selections

Since the expected voltage levels described in [1] are very low, a voltage multiplier is necessary in order to achieve a respectable charge output. In Section 2.2.4, it was made clear that the Villard/Greinacher configuration (also referred to as the Cockroft-Walton multiplier) holds a distinct advantage over the Dickson charge pump alternative, in that no additional support circuitry is required. The Dickson configuration is also primarily intended for DC applications, which this work is not.

As discussed in Section 2.2.4, the six-diode Villard multiplier will be employed, along with a peak detector-based rectifying stage at the multiplier's output (resulting in a Greinacher Rectifier). This has been shown to be the optimal trade-off point between the number of stages and overall circuit efficiency[19]. The resulting DC voltage (in theory 6 times greater than the input voltage) will be the source of charge accumulation for an arbitrary energy storage element.

Owing to their lower junction threshold voltages and quicker response times (described in Section 2.2.4), low-capacitance Schottky diodes will be used. This has also been done in several of the referenced works, including [5], [8], [19], [15].

3.7 – Performance Targets

Firstly, the design must fit within the 6cm x 6cm (or 3600mm^2) frame that is common among the existing works compared in Table 1. 6cm x 6cm is also size of PCB that could easily fit into the casing of common scientific calculators, such as the Texas Instruments TI-30Xa[15] or within common household thermometer/hygrometers offerings. Evidently, a

[15] Product details available at: http://education.ti.com/en/us/products/calculators/

smaller design is ideal, for simplified placement into more size-restricted portable electronic devices.

A power conversion efficiency of greater than 20% is desired in order to remain competitive with the existing works. Mobiles typically use rail voltages of 1.8V, 2.5V and 2.8V for various sub-circuits [39].

The targeted frequency bands (for which excellent return loss and an omni-directional radiation pattern will sought) will include the 850MHz cellular band, 1900MHz PCS band and 2.4GHz Wi-Fi bands. Where possible, the 900MHz cellular and 2.3GHz WiMax bands will be included in order to achieve maximum voltage.

3.8 – Conclusion

In this chapter, different design considerations regarding the rectenna system have been discussed including selections of antenna and rectifier topologies. The selections were justified based on references presented in Chapter 2. The next chapter will resume the design itself and the simulated results we obtained.

Chapter 4 – Design and Results

The following sections describe the design process, commencing with the simulation and optimization of the voltage multiplying/rectifying circuit in Agilent's Advanced Design System (ADS)[16]. Next, the design of the antenna will be detailed, including the co-simulation using ADS and Agilent's 2.5D EM solver, Momentum. For this exercise, we assume a fixed load consisting of a super capacitive/resistive load combination, which is a viable charge storage medium for wireless sensors.

4.1 – Rectifying Element Design

There are several steps to the rectifier design, comprising device selection, rectifier layout, circuit source pull, target impedance point selection and unconditional stability analysis. This will provide the target impedance for the antenna portion, to complete the rectenna design.

4.1.1 – Device Selection

There are many Schottky diodes available on the market today, though not all are suitable for the frequency ranges and low expected input power levels targeted in this work.

The devices that stood out after a scan of the market included the SMS7621 and SMS7630 from Skyworks, as well as the MA4E2054 from M/ACom, the 1PSxSB17 series from Philips/NXP and the HSMS-2850 from Agilent Technologies. A comparison of key operating characteristics is contained in Table *3*. In this table, V_F is the forward voltage drop across the diode junction, BV represents the reverse junction breakdown voltage, I_F is the rated continuous forward current, I_S represents the saturation current and C_T indicates the total diode capacitance (including junction, overlay and package capacitances).

[16] Agilent Technologies Inc. (2008). Advanced Design System (Version 2008.200). (Computer Software). University of Ottawa (Legacy). Retrieved 2011. Now replaced by more recent version of ADS, available from http://www.home.agilent.com/en/pc-1297113/advanced-design-system-ads?&cc=CA&lc=eng

Table 3 - Comparison of Schottky Diodes

Model	V_F @ 0.1mA	V_F @ 1mA	BV	I_f	I_S	C_T
SMS7621	n/a	260-320mV	3 V	50mA	40nA	0.25pF @ 0V
SMS7630	**60-120 mV**	**135-240mV**	2 V	50mA	5000nA	0.30pF @ 0.15V
MA4E2054	n/a	250-350mV	5 V	20mA	30nA	0.30pF @ 0V
HSMS-2850	150mV	250mV	3.8 V	50mA	3000nA	0.30pF @ 0.5V to -1.0V
1PS76SB17	300-350mV	360-450mV	n/a	30mA	n/a	0.80pF @ 0V

Due to its extremely low threshold voltage, the SMS7630 diode was an easy choice for this design. The diode is offered by the manufacturer in several packages, both in single and dual configurations. Although Villard voltage doublers (and Greinacher rectifiers) employ multiples of two diodes, the single configuration (SC-79 package) offers more footprint and layout flexibility as two individual units, when compared to the SC-70 dual package. Therefore, the SC-79 single diodes will be used.

4.1.2 – Rectifier Layout

Firstly, the initial microstrip layout is created in order to enable mounting Surface Mount Technology (SMT) devices and sustaining proper current flow. A material stack-up such as the one shown in Figure 26 will be used.

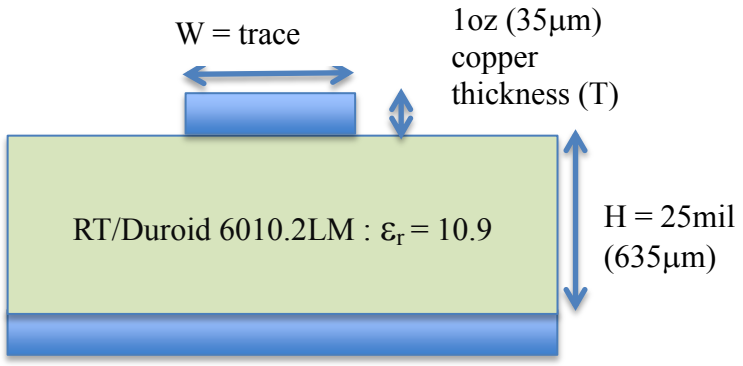

Figure 26 - Microstrip Stackup

It includes two copper layers (of 35µm thickness) separated by a thin 635 µm (25mil) layer of dielectric substrate (Rogers RT/duroid 6010.2LM). It is commonly known that as the dielectric constant of the substrate used in a microstrip implementation is increased, the length of line required to achieve a given electrical length is reduced. Thus, a substrate with a high dielectric constant, such as the RT/duroid 6010.2LM laminate from Rogers Corporation will be used for the design. In comparison to FR-4 (ε_r = 4.5 to 4.6), which is the substrate selected in many of the references, the RT/duroid 6010.2LM (design ε_r of 10.9) allows the size reductions shown in Table *4*.

Other substrate parameters used in the simulation were the relative permeability (*Mur* = 1), the trace conductivity (*Cond* = 1.0 x 10^{50} S/m) and the dielectric loss tangent (*TanD* = 0.0023). Parameter values were selected based on the substrate datasheet from Rogers Corporation [40].

Microstrip dimension values were quickly calculated using Agilent's LineCalc tool in ADS. The unsurprising result is a 54% reduction in 50Ω trace width and >30% reduction in required line length to implement a full wavelength in microstrip.

Table 4 - Effect of Dielectric Selection on Circuit Dimensions

Material	**ε_r (typical)**	**Tan δ**	**50Ω Line Width**	**λ Line Length (2.4GHz)**
FR-4 (H=25mil)	4.5 to 4.6	0.0018	1.1557mm=45.50mils	68.30mm=2689mils
RT/duroid 6010.2LM (H=25mil)	10.9	0.0023	0.5223mm=20.56mils	47.33mm=1863mils

For our targeted working frequencies, the microstrip values (analytically calculated from the equations reported in [Appendix A] are summarized in Table *5*.

Table 5 - Target Microstrip Dimensions at Working Frequencies *for* Z_0=50Ω

Frequency	**50Ω Line Width**	**λ Line Length**
2.45GHz	0.5223mm=20.56mils	46.36mm=1825mils
881.7MHz (Center of downlink band for GSM band)	0.5229mm=20.59mils	129.26mm=5089mils
1960MHz (Center of downlink band for PCS band)	0.5224mm=20.57mils	58.01mm=2284mils

The circuit was first constructed at the schematic level in ADS, with all transmission lines having a width of 0.5334mm = 21mils, leading to a characteristic impedance near 50 Ω. The width was rounded up from the ideal values in Table *5* in order to remain in line with realistic manufacturing tolerances. Landing pads were also created for each of the discrete components, following manufacturer recommendations (0.76mm x 0.5mm) from the appropriate datasheets. Care was also taken to model the step transitions from 50Ω lines to wider pad widths, thereby taking the discontinuity into account for S-parameter calculations.

The manufacturer's SPICE diode model (see Figure 27) and appropriate lumped capacitor elements were used in the S-parameter simulation. The capacitors used were 24pF, providing adequate and intermediate charge storage with quick charge times and minimal voltage drop across the voltage multiplier section.

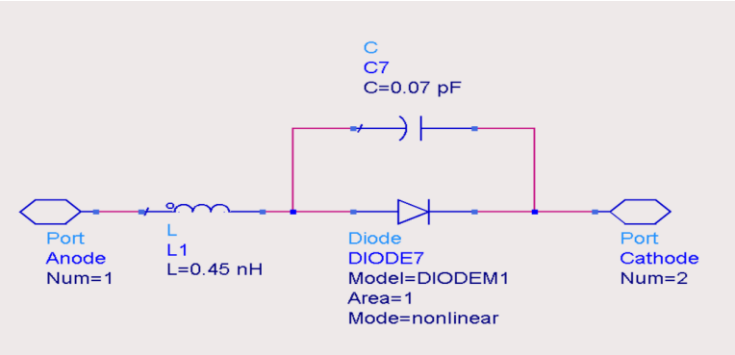

Figure 27 - SPICE Model for SMS7630 Diode

The voltage drop from the ideal expected output voltage of this configuration can be calculated as shown in Equation 7, where I_L is the current provided to the load, f is the operating frequency in Hz, C is the capacity of the capacitors and n is the number of two-element stages in the multiplier.

Equation 7

$$\Delta V = \frac{I_L}{fC}\left(\frac{2}{3}n^3 + \frac{1}{2}n^2 - \frac{1}{6}n\right)$$

In this case, assuming a load current of 0.1mA, operating frequency of 881.7MHz, 24pF capacitor selection and n=3, the result would be a 19.25mV drop from the expected output value. Subtracting this value and the worst-case junction drop from the final peak detector diode, the expected output voltage should be:

$$v_{out} = 6 \cdot v_{in} - 19.25mV - 120mV$$

Microstrip transmission line models were also implemented to form a circuit ready

for eventual fabrication. These changes all served to bring the simulation results closer to real world performance. Next, a layout was generated and simulated in Momentum. The EM results were then used in a co-simulation to achieve more accurate results, as shown in Figure 28.

The landing pads for the capacitors and Schottky diodes are the wider segments of transmission line on either side of each transmission line gap.

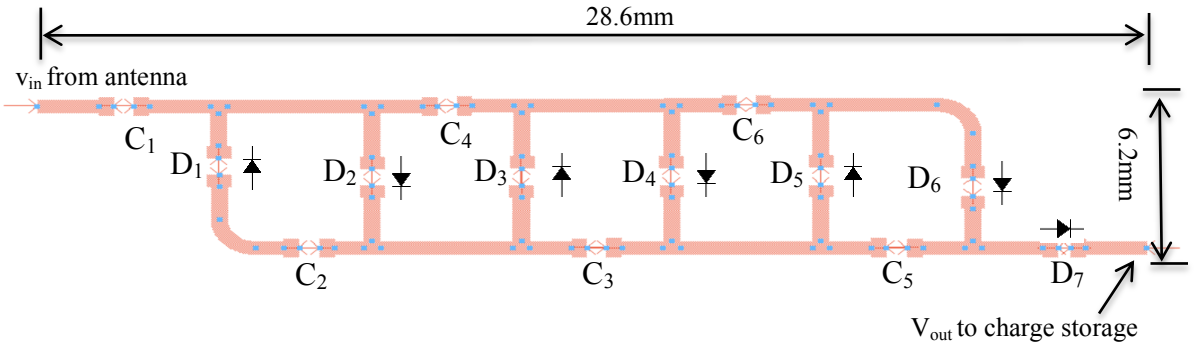

Figure 28 - Co-Simulation Setup w/ Copper Model Included

The gaps are intentionally created by removing discrete lumped components from the layout. This is done in order to include internal simulation ports at each landing pad. The results of the Momentum simulation are presented as a multiport file, which can be linked to a circuit look-alike model that provides a visual representation of the copper simulated. This facilitates integration of both copper and discrete lumped components into an S-parameter co-simulation in ADS.

4.1.3 – Circuit Source Pull

'Source pulling' (a process akin to the more commonly discussed 'load pull') is the process of methodically varying the impedance that the source presents to the input of the network being analyzed and recording key performance parameters at each impedance point. In our case, these parameters are power conversion efficiency and power level delivered to

the load. The concept was initially introduced in 1984, by Bava [40] and has seen extensive use in both low noise amplifier (LNA) and power amplifier (PA) characterization and design.

The results of the variations are typically plotted on a *Smith Chart*. The individual points on the plot can then be grouped; forming concentric regions of performance level. This is done for all parameters of interest (power efficiency, power delivered to the load) and an optimal trade-off is selected between all measured parameters, which may not necessarily be simultaneously optimized at a given impedance point. The resulting impedance selection is the target source impedance for the design. In the case of this design, this impedance will be the design target for the antenna network's output impedance, as seen by the input of the rectifier circuit.

In order to accomplish the source pull simulation, a single tone Harmonic Balance simulation was set up in ADS, based on a trusted vendor-supplied test bench template. The use of a parameterized source impedance to allow the creation of the desired source pull contours. Source pull contours were then created for power conversion efficiency (RF to DC) and for power level delivered to the load at various input power levels.

In order to achieve a proper input impedance selection, care was taken to emulate a charge storage element and load, represented by a Panasonic Gold 4.7F super capacitor and a 320Ω load. A super capacitor is made using a completely different manufacturing process than a traditional capacitor. While a standard capacitor consists of two parallel plates separated by a dielectric (shown on the left-hand side of Figure 29), a supercapacitor uses a porous medium to achieve the equivalent of two parallel electrodes with immense surface area (the composition of an electrochemical double layer capacitor, a type of supercapacitor, is shown on the right-hand side of Figure 29). This arrangement avoids the physical limitations (plate spacing and limited surface area) of a traditional capacitor and enables significantly higher charge capacity. This is desirable in an energy harvesting application intended for small low-power consumer since it can have sufficient capacity to completely

replace a chemical battery. This component also offers fast charge/discharge time, long-term stability and a low level of heating during operation.

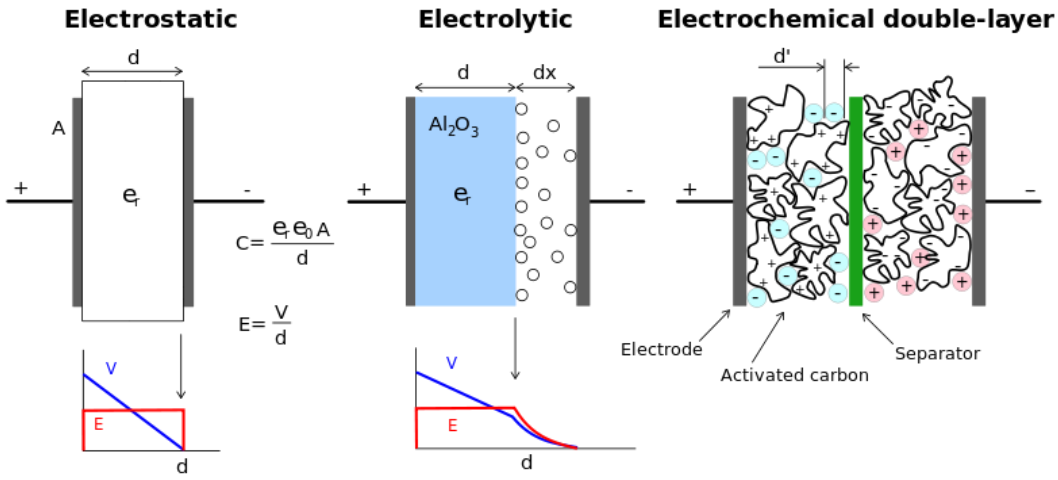

Figure 29 - Capacitor and Supercapacitor Compositions[17]

The equivalent circuit chosen to represent the super-capacitor was the 'Simplified' model noted in [43] and shown in Figure 30. Included (in addition to the ideal capacitance, C_S) are an equivalent series resistance (R_S) representing package lead losses as well as a parallel resistance (R_p) representing the leakage current through the activated carbon shown in Figure 29.

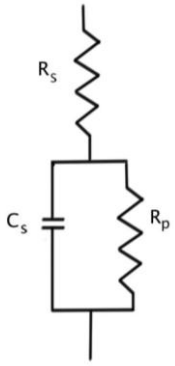

Figure 30 – Super-capacitor Equivalent Circuit

[17] Stan Zurek, *Supercapacitor_diagram.svg,* Retrieved November 2012 from Wikimedia Commons at http://en.wikipedia.org/wiki/File:Supercapacitor_diagram.svg

The values found experimentally in [43] for the model parameters were used for the current work as well, as depicted in Table *6*.

Table 6 – Super-Capacitor Equivalent Circuit Parameters

Parameter	Value
R_S	0.80Ω
C_S	4.06F
R_P	2.01kΩ

The equivalent impedance for the equivalent circuit was then found to be:

Equation 8

$$Z_{eq} = R_S + \left(j\omega C + \frac{1}{R_P}\right)^{-1}$$

A simple Octave[18] script (an alternative to Matlab) was written to automate the impedance calculation for the first fundamental frequency (881.7MHz), as well as the first four harmonics (Appendix B). The results are shown in Table *7*.

Table 7 - Equivalent Impedance of super-capacitor (881.7MHz and Harmonics)

Frequency (GHz)	Z_{eq} (Ω)
0.8817	$0.8 - j4.4460 \times 10^{-11}$
1.7634	$0.8 - j2.2230 \times 10^{-11}$
2.6451	$0.8 - j1.4820 \times 10^{-11}$
3.5268	$0.8 - j1.1115 \times 10^{-11}$
4.4085	$0.8 - j8.8921 \times 10^{-12}$

[18] GNU Octave (Version 3.4.0). (Open source computer software). Retrieved June 2012. Available from http://www.gnu.org/software/octave/

With these known impedances, the source pull simulation was performed and the resulting performance was plotted (see Figure 31), in which the power added efficiency was defined as:

Equation 9 $$PAE(\%) = 100\left(P_{DL(watts)} - P_{AVS(watts)}\right)$$

and where P_{DL} is the power delivered to the load and P_{AVS} is the power available from the source.

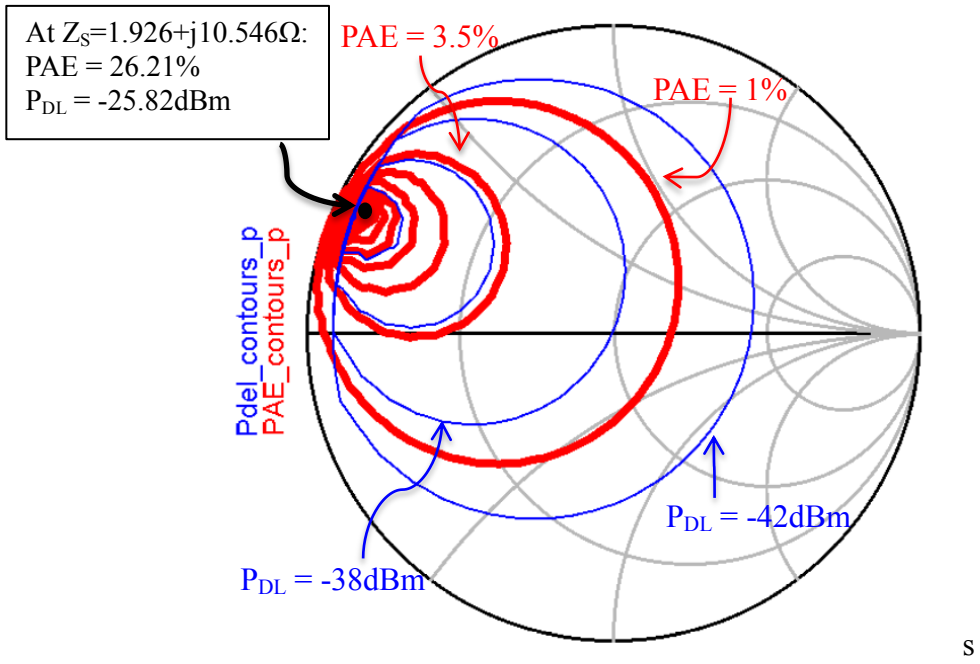

Figure 31 - Source Pull Contours for Greinacher Circuit

The contours show that both the *PAE* and P_{DL} are maximized in the upper left (inductive) quadrant of the Smith Chart. The impedance point selected as **Z_S=1.926 + j 10.546 Ω.** This impedance provided a best-case simulated power added efficiency (*PAE*) of 26.44%, with -15.78dBm delivered to the load from a -10dBm source.

As expected, and as seen in many of the other works in this field, efficiency drops off

slightly as input power decreases and currents through the diodes fall away from the saturation point. Figure 32 and Figure 33 illustrate the simulated efficiency and power delivered to the load, respectively, as functions of the power available from the source (P_{AVS}).

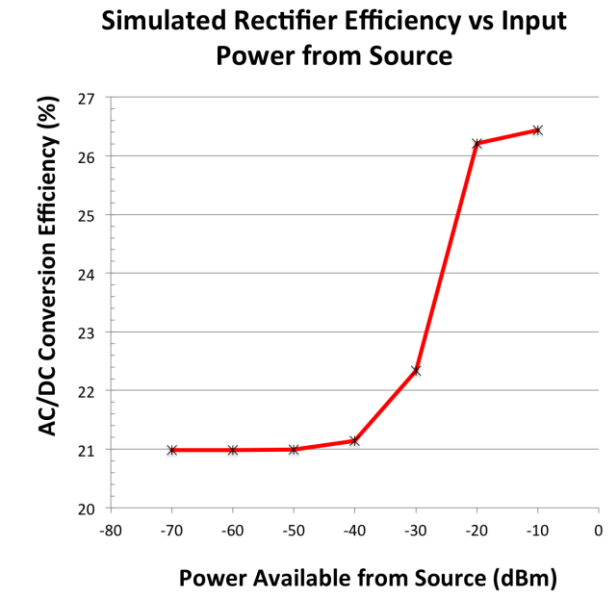

Figure 32 - Simulated Efficiency vs P_{avs}

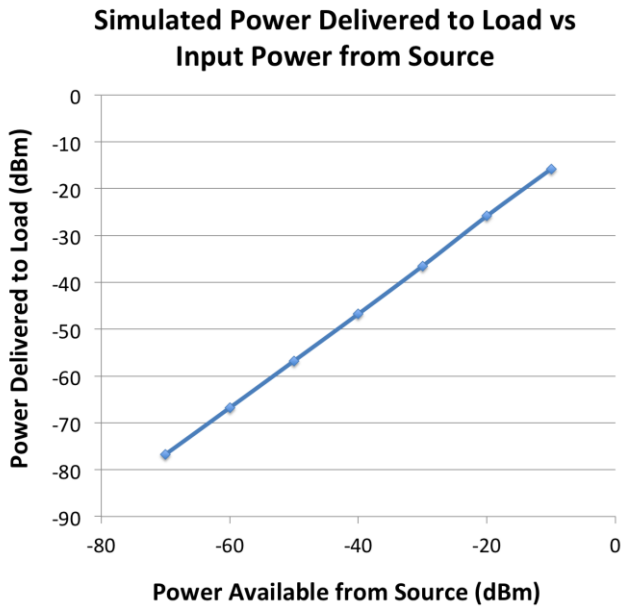

Figure 33 - Simulated Power Delivered to Load vs P_{avs}

The power-added efficiency results meet the target requirement of >20% set in Section 3.7 and were thus accepted for the design.

4.1.4 – Unconditional Stability Analysis

Before moving further, an S-parameter-based stability analysis was performed, using both the Rollet Stability Factor (*K*) and the Stability Measure (*b*), defined in [44] as complimentary tests for unconditional stability. Even though only diodes and capacitors are included in this circuit, stability analysis is performed to rule out the presence of unintended negative resistance oscillators (a possible result from these components), as discussed in [23].

The Rollet Stability Factor must stay above 1 for the studied frequency range. It is computed as:

Equation 10
$$K = \frac{1-|S_{11}|^2-|S_{22}|^2+|S_{11}*S_{22}-S_{12}*S_{21}|^2}{2*|S_{12}*S_{21}|}$$

As an additional condition, the stability measure must remain positive. It is calculated as:

Equation 11
$$b = 1 + |S_{11}|^2 - |S_{22}|^2 - |S_{11} * S_{22} - S_{12} * S_{21}|^2$$

In both cases, the simulation values remained within the aforementioned limits across the studied frequency range of 100MHz - 5GHz, thereby guaranteeing unconditional stability in this range. These results, along with the highlighted threshold values are displayed in Figure 34.

With the now completed rectifier ready for integration into a full harvesting system, a reception antenna needed to be designed at 881.7MHz.

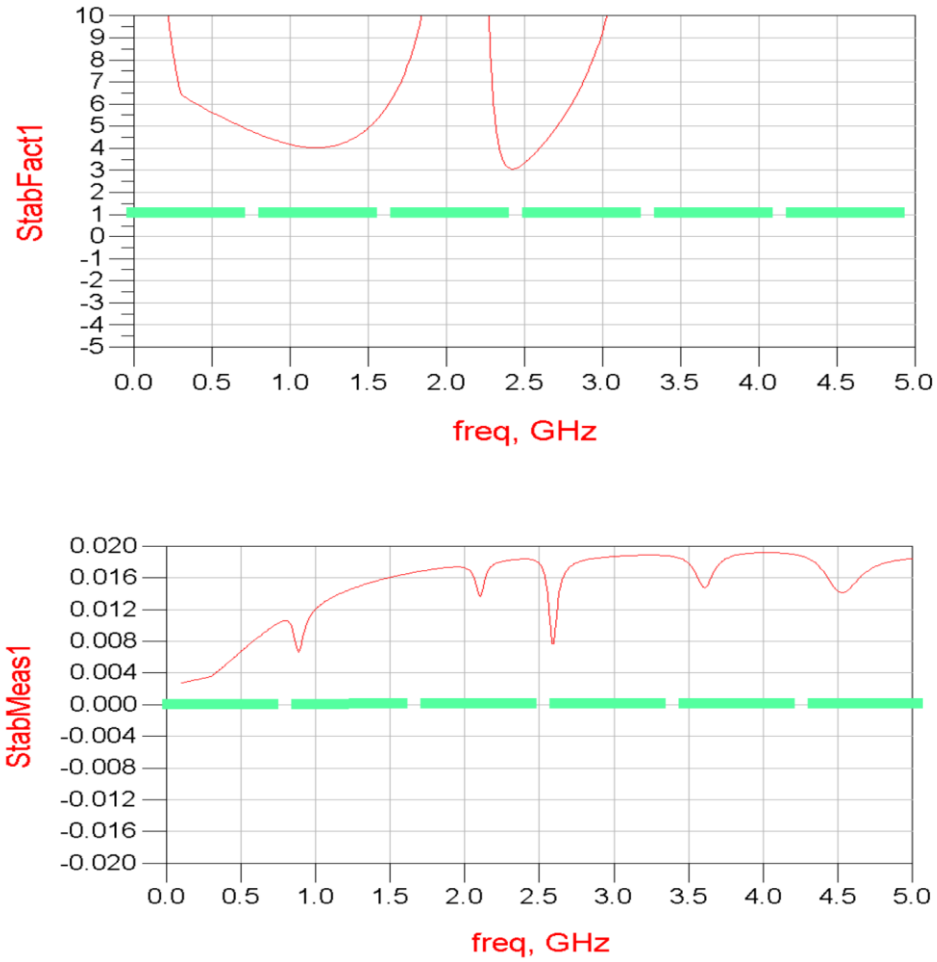

Figure 34 - Stability Test Results Showing Unconditional Stability of Rectifier

4.2 – Antenna Design

The antenna type selected in Section 3.7 is a Koch fractal loop, which provides good multiband performance, with minimal physical dimensions and also allows a convenient feed point for connection to the rectification circuit. The reference [32] does not fully match the frequency plan targeted in this work, so modifications will be required for antenna dimensions and configuration in order to hit the proper resonance points, while matching the source impedance (Z_S=1.926 + j 10.546 Ω) found in Section 4.1.3. Prior to any new simulations, a verification simulation was completed with an Agilent reference design to ensure proper simulation environment behaviour (see Figure 35). Measurements performed by Agilent Technologies Inc. and provided with ADS software tutorial are shown in red. The blue trace, shown with markers, is a result of the Momentum simulation run for this work and adequately approximates the measurement results.

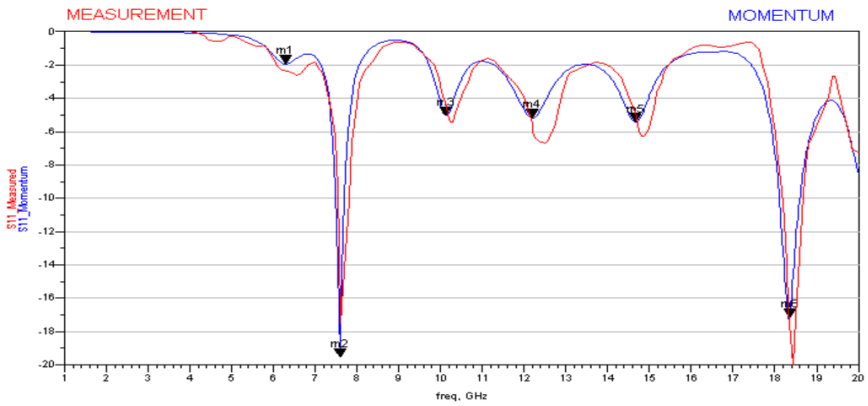

Figure 35 - Verification of Reference Design Simulation
(Agilent measurements shown in red, simulation shown in blue, with markers)

4.2.1 – Initial Antenna Design Calculations

Now that the target values for line width and guide wavelength λ are known, we can begin the design of the physical layout. If one were to implement a full wavelength loop as a

circle, the occupied area for the largest case, at the target frequency of 881.7MHz, we would have a target circumference of 1λ. At thus frequency, 1λ = 129.26mm, as shown in Table *5*. Thus we have the following dimensions:

$$radius\ (r) = 20.57mm \qquad area = \pi r^2 = 1329.6mm^2$$

A sketch of the loop is shown in Figure 36.

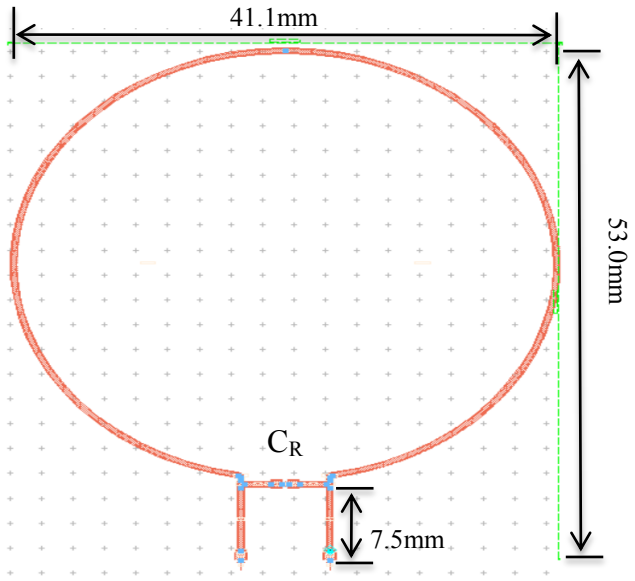

Figure 36 - Copper Layout for 881.7MHz Loop Antenna

In the above loop, the spacing between the two feed branches was determined based on the results from [45], showing that fringing fields remain relatively unaffected by adjacent transmission lines, as long as the separation distance is approximately 3 times the substrate height (3 x 0.635mm = 1.905mm). The result was rounded up to 2mm. The capacitor (C_R) added to achieve the desired resonance at 881.7MHz was selected based on the assumption that the desired input impedance for the antenna had been achieved (i.e. 1.926+j10.546Ω).

The target was thus to counteract the reactive component of the antenna impedance at the target frequency.

Equation 12

$$C_R = \frac{1}{2\pi f} * \frac{X_L}{{R_L}^2 + {X_L}^2} = 16.56pF$$

This first antenna will serve as an additional simulation reference point for later antenna simulations.

We next attempt a different antenna topology, an end loading equilateral hexagon (as used in [32]). The area of a hexagon is computed by dividing the shape into 6 equilateral triangles (Figure 18).

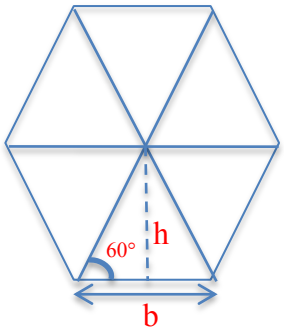

Figure 37 - Area of a Hexagon

and computing the area of one of the triangles as:

$$A_{triangle} = \frac{b \times h}{2} = \frac{b^2 sin60^\circ}{2} \quad \rightarrow \quad b = \frac{129.26mm}{6} = 21.543mm$$

$$A_{hexagon} = 6 \cdot A_{triangle} = 6 \cdot 200.97mm^2 = 1205.77mm^2$$

This can be reduced by applying a Koch fractal transformation to each segment of the hexagon, as described in Section 2.2.1, resulting in 24 sub-segments of equal length. Each sub-segment of this transformation would have a length of 129.26mm ÷ 24=5.3858mm.

Using the same method to calculate the area of the inner hexagon (albeit with new value for b), the 6 small equilateral triangles along the periphery have their areas added to the total. The result is 753.62mm^2, for a 37.5% decrease in area from the starting shape.

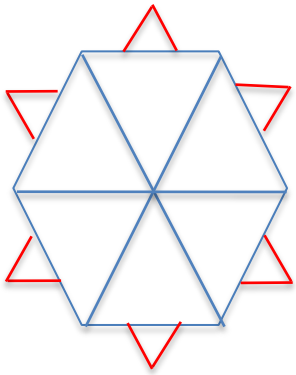

Figure 38 - Result of First Koch Iteration

4.2.2 – Antenna Simulation Results

The initial design was a simple full-wavelength loop for the first target frequency, 881.7MHz. Firstly, in an ADS schematic-based S-parameter simulation, the return loss ($|S_{11}|$) was calculated and optimized to be matched to Z_{in}=1.926+j10.546Ω, with results shown in Figure 39. The total length of the loop was roughly 1.06 times the expected full wavelength calculated in Table *5*.

In simulation, the capacitance value for C_R needed to be adjusted down to 8.2pF, which may be partially explained by the mutual capacitance between the feed lines that would lie in parallel with the capacitor. This was not expressly modeled in the schematic-based simulation. As the return loss simulation results were promising, the accuracy of the design was furthered by performing both a 2.5D EM simulation and an ensuing co-simulation with the resulting copper model shown in Figure 36.

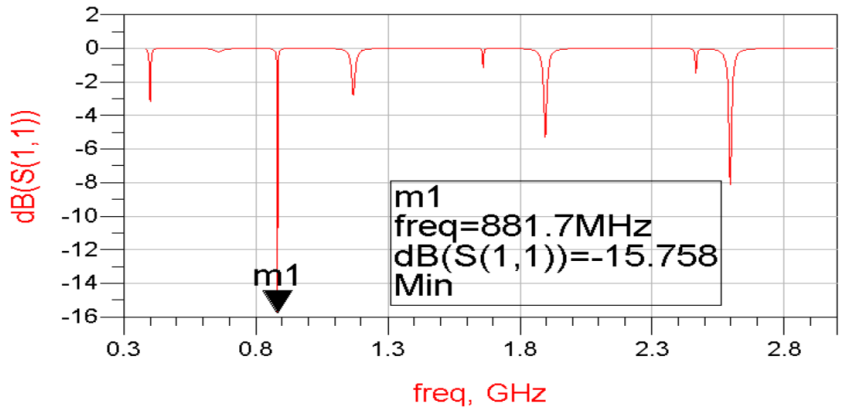

Figure 39 - Return Loss Results for Simple Loop Antenna (Schematic Only)

The far field radiation pattern from the EM simulation followed the expected distribution for a full wavelength circular loop[46], as shown in Figure 40. This is a fairly directional result that would not serve very well in a handheld consumer device application, due to sharp gain drop-off outside the main lobe in the broadside direction.

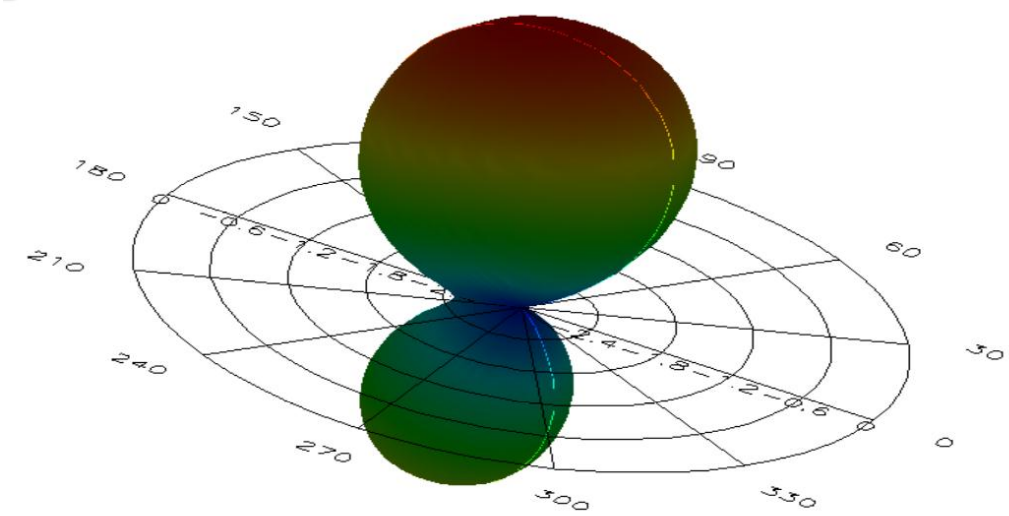

Figure 40 - Far Field Radiation Pattern for Designed Full Wavelength Loop at 881.7MHz

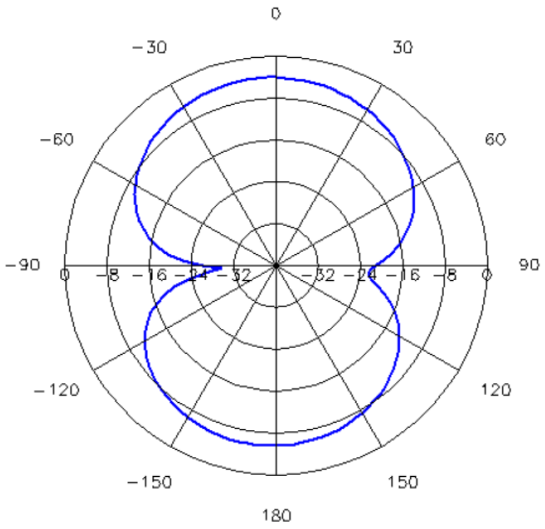

Figure 41 - Loop Co-Polarization (ϕ=0° Plane)

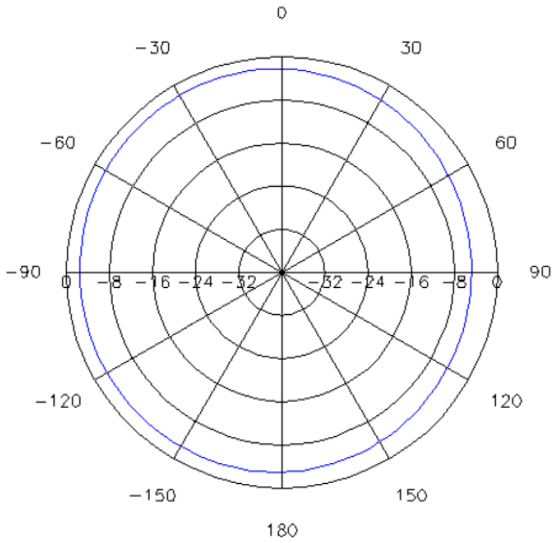

Figure 42 - Loop Co-Polarization (ϕ=90° Plane)

Although not an ideal candidate for this application, the simulation of the simple loop antenna at 881.7MHz has provided an additional reference point to add confidence to later simulation results.

Next, a Koch fractal antenna fitting the dimensional requirements was simulated (see Figure 44). Beginning with the same overall length, a hexagon was formed and transformed, as described in Sections 2.2.1 and 4.2.2. Optimization of the segment length and resonant capacitor values was necessary to counteract changes in the antenna geometry. After fine-tuning, the schematic simulation produced the return loss results shown in Figure 22.

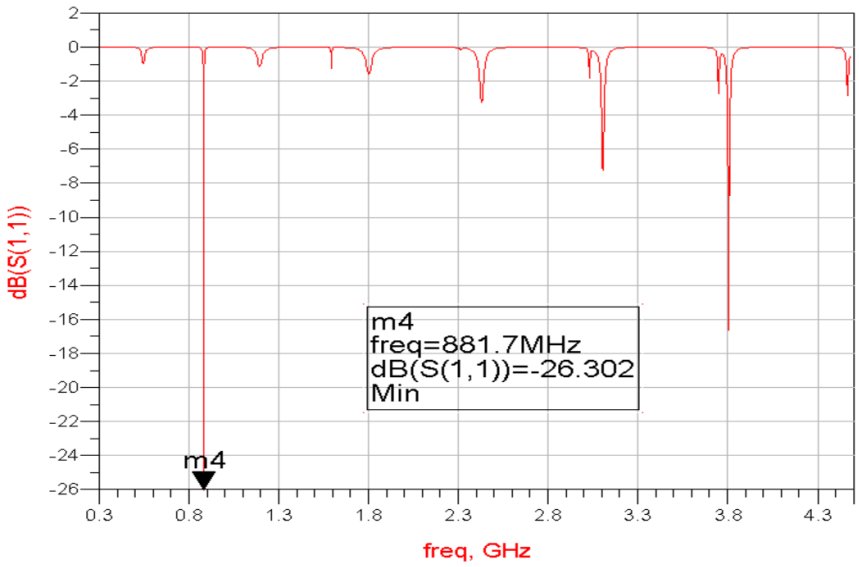

Figure 43 - Wideband Return Loss for Koch Loop Using Schematic Simulation

When a copper layout was generated from this circuit, the overall occupied area was 1794mm^2. This result fits within the target design space of 6cmx6cm=3600mm^2.

The full-wave EM simulation was then completed in Momentum, with the copper layout shown in Figure 44. There was an approximate 15MHz shift in overall response upon co-simulation, as well as degraded, but still acceptable, return loss minimum, seen in Figure 45. This can be attributed in part to the mutual capacitance between adjacent microstrip segments and the inclusion of higher order mode effect, which are not accounted for in transmission line theory.

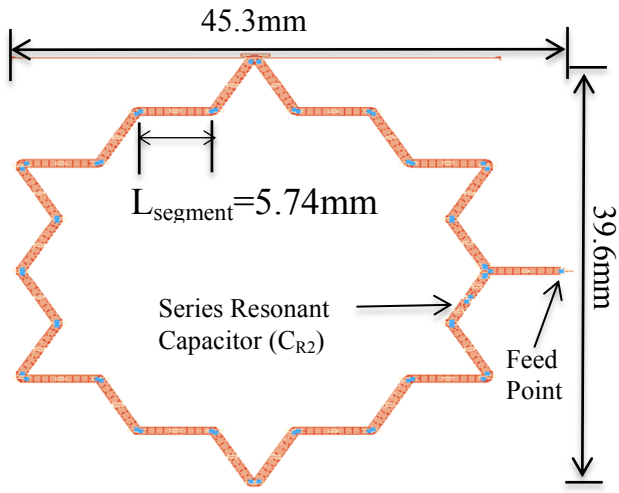

Figure 44 - Simulated Copper Layout (Single Koch Loop)

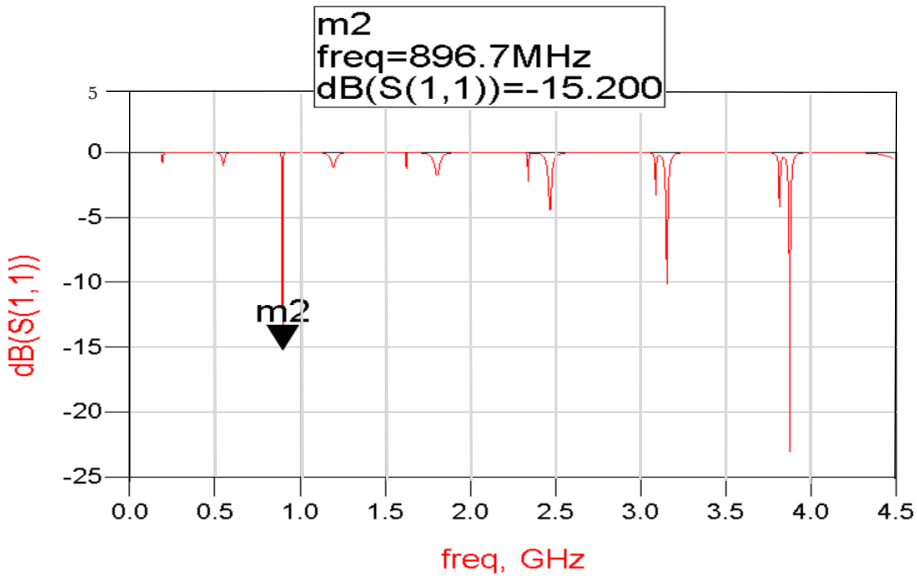

Figure 45 - Return Loss from Momentum Co-Simulation

The layout and values of the resonant capacitor (C_{R2}) were adjusted to compensate for the frequency offset. The segment length was reduced to 5.74mm, while C_{R2} was reduced to 3.5pF. At the same time, useful, though less pronounced resonances were established in the 1.8GHz and 2.45GHz regions, both busy bands for DCS and Wi-Fi, respectively (Figure 46). The 3.1GHz radiolocation band is also included.

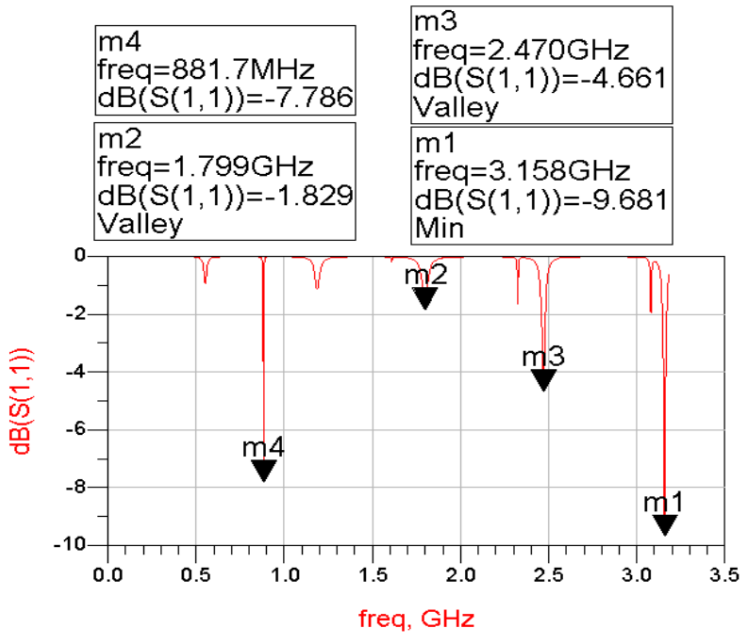

Figure 46 - Results of Copper Adjustment to Initial Koch Loop

The radiation pattern at 881.7MHz was plotted using EMDS[19], resulting in the three dimensional visualization shown in Figure 47 and the polar plots shown in Figure 48 and Figure 31.

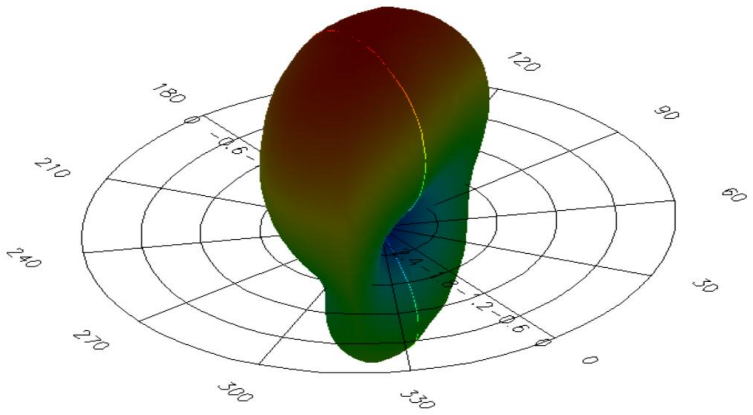

Figure 47 - Radiation Pattern for Initial Koch Loop

[19] Agilent Technologies Inc. EMDS for ADS 2008. (Version 2008.200). (Computer software). University of Ottawa (Legacy). Retrieved 2011. Now replaced by EMPro 3D, available from http://www.home.agilent.com/en/pc-1297143/empro-3d-em-simulation-software?nid=-34278.0&cc=CA&lc=eng

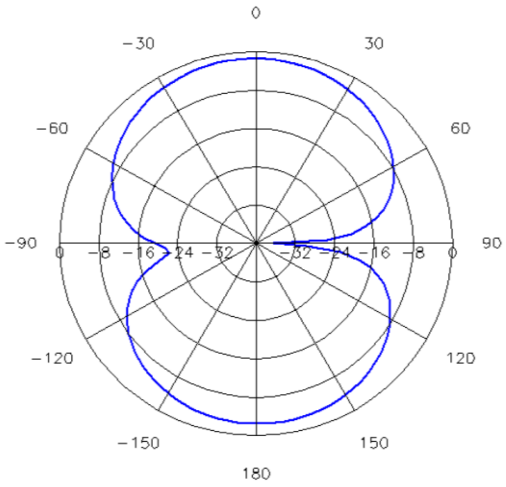

Figure 48 – Koch Loop Co-Polarization (ϕ=0° Plane)

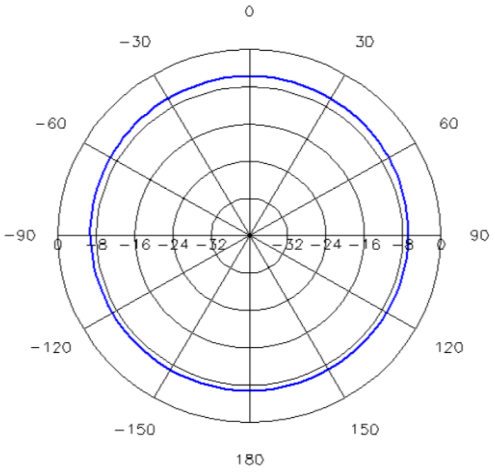

Figure 49 – Koch Loop Co-Polarization (ϕ=90° Plane)

The radiation pattern has a slightly broader main lobe, but still does not achieve the ideal omnidirectional pattern targeted. A new iteration was required.

In an effort to improve the radiation pattern as well as enhance antenna bandwidth and improve performance in multiple frequency bands, a layout similar to that found in [32] was designed with this work's target frequencies in mind. The new substrate necessitated very different segment lengths. Figure 50 illustrates the ADS schematic and Momentum Layout, respectively, for the antenna.

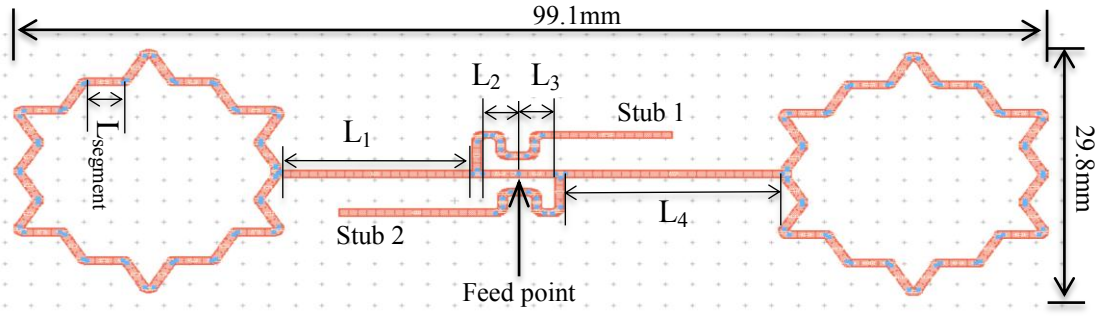

Figure 50 - Momentum Layout for Multi-Frequency Antenna Based on [32]

The Koch loops on either end of the structure aim to target the 881.7MHz cellular band. These were created by starting with the total length needed for a full wavelength 129.26mm, subtracting the feed distance (L_1+L_2=22.2mm) and dividing the remaining distance among the segments of the Koch Loop.

Since there are 24 segments, as well as angles (6 of 120° and 18 of 60°) to consider, the following equation provides the total length of the loop:

Equation 13 $$L_{LoopTotal} = 24\left(L_{segment}\right) + 6\left(\frac{2\pi r}{3}\right) + 18\left(\frac{2\pi r}{6}\right)$$

where r is the radius of the angle, which is kept at half of the microstrip line width, in order to maintain symmetry. Thus, in the case of Figure 50, we would have $L_{segment}$=3.45mm and r=0.477mm, giving a result: L_{Total}=97.78mm, which added to the feed length of 22.2mm gives 120.0mm. The missing distance from the ideal expected result can be explained by the modification of line impedance courtesy of the attached stub along the feed line path.

An interesting point to note is that this shape (or any n-th order Koch fractal polygon transformation) can be completely described by the segment length and transmission line width. Thus, subtracting and feed length from the theoretical electrical length desired, the remainder can be used as a variable in an automated geometry generation. Assuming a hexagon, as in this work, we can re-arrange Equation 13:

$$L_{segment} = \frac{\left(L_{LoopTotal}\right) - 6\left(\frac{2\pi r}{3}\right) - 18\left(\frac{2\pi r}{6}\right)}{24}$$

Extending this to an arbitrary polygon with N sides, we obtain Equation 14:

Equation 14 $$L_{segment} = \frac{\left(L_{LoopTotal}\right) - N\left(\frac{2\pi r}{3}\right) - 2N\left(\frac{2\pi r}{6}\right) - N\left(\frac{2\pi r}{N}\right)}{4N}$$

This type of scalability permits setting the segment length ($L_{segment}$) as variable in the ADS simulation, which can be parameterized and quickly changed to address a new principal frequency band for a given polygon without changing the outer shape or symmetry.

Returning to the design, two meandered $\lambda/2$ stubs of at 1960MHz were added at approximately 3.5mm (or $\lambda/12$ at 2.45GHz) on either direction from the center feed point. These will add a resonance in the desirable PCS band. The meandering and mirroring the stubs on either side of the main axis were done to minimize occupied area.

After optimization for best return loss performance, the line width used throughout this antenna layout was set at 0.954mm (or a characteristic impedance of approximately 37Ω on the selected substrate. Measurements from Figure 50 are listed in Table 8:

Table 8 - Dimensions of Multi-Frequency Antenna

Measure	**Value**
$L_{segment}$	3.45 mm = 136 mils
L_1	18.7 mm = 736 mils
L_2	3.5 mm = 138 mils
L_3	3.5 mm = 138 mils
L_4	20.8 mm = 820 mils
W_{Stub1}	0.954 mm = 38mils
L_{Stub1}	26.37 mm = 1038 mils
W_{Stub2}	0.954 mm = 38mils
L_{Stub2}	28.88 mm = 1137mils

The linear S-parameter simulation for this design produced the desired return loss valleys in the cellular, PCS and Wi-Fi bands, as shown in Figure 51, making the antenna useful for multiband applications.

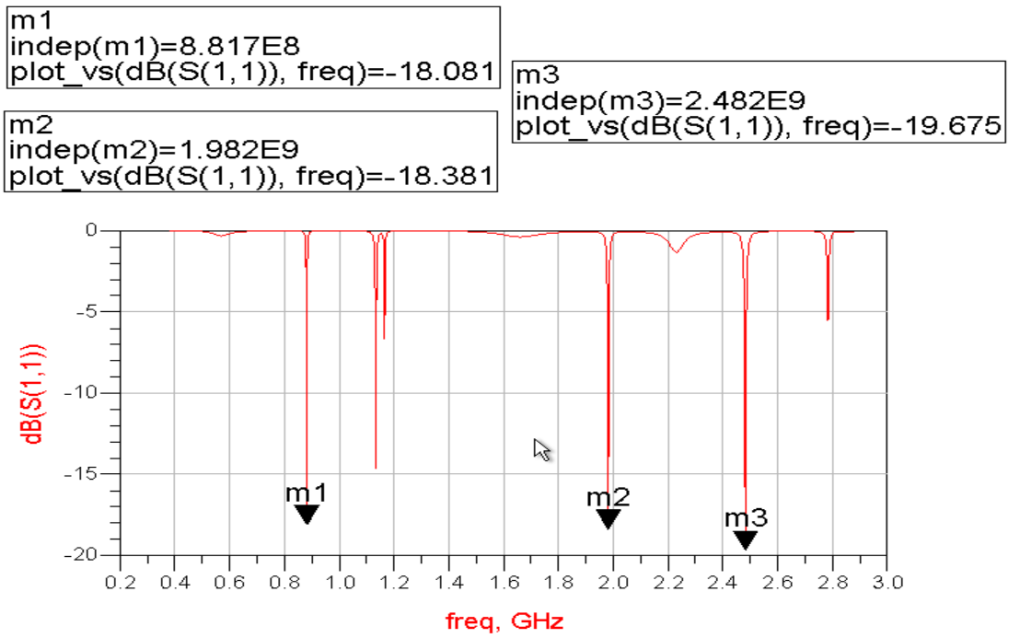

Figure 51 - S11 Results for Multi-Frequency Antenna

Simulation of the radiation pattern in Momentum produced similar results to previous antennas simulated in this work, though with different null orientation in the x-y plane and slightly more directivity. This is less desirable as it strays from the intended goal of an omnidirectional radiation pattern (and thus minimal directivity).

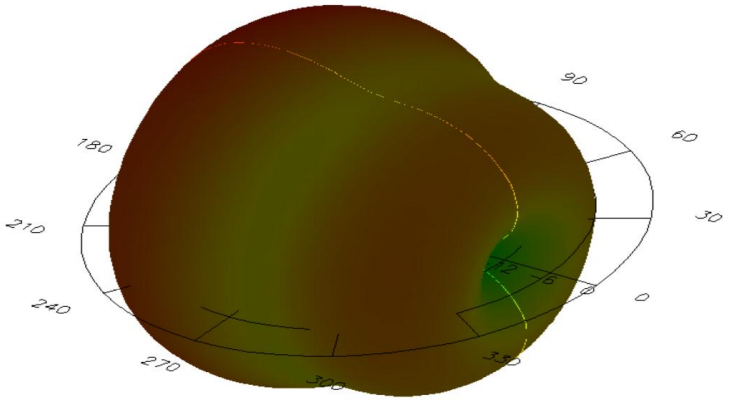

Figure 52 - Simulated Radiation Pattern for Multi-Frequency Antenna

The variations in null orientation are more evident in the 2-D polar representation of the results, seen in Figure 53. Figure 54 also shows a retraction of the radiation pattern at the ϕ=90° cut. The orientation of the nulls is less troublesome than the directivity increase, as their orientation in any eventual personal consumer device is not fully predictable.

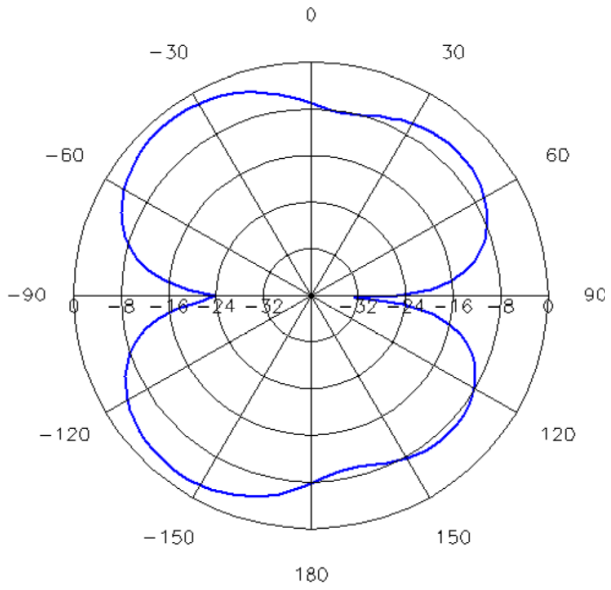

Figure 53 – Co-Polarization (ϕ=0° Plane)

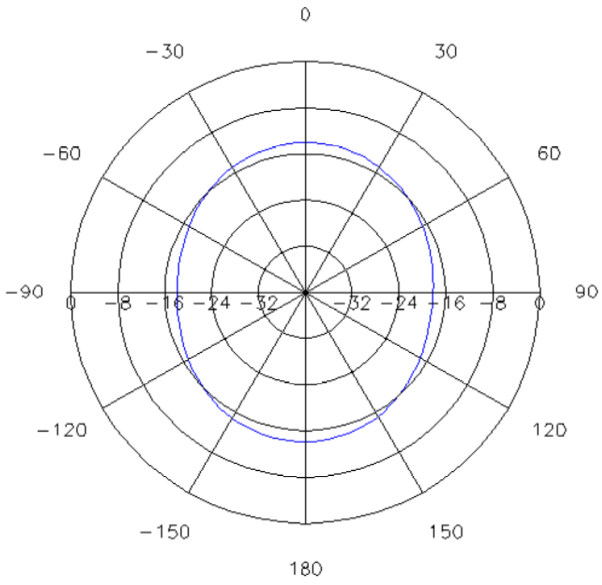

Figure 54 - Co-Polarization (ϕ=90° Plane)

The antenna was further modified to reduce its size, which (at 2951mm^2) had only barely met the specification set out in Section 3.7. Included were more compact tuning stubs, and increased utilisation of meandering via the Koch fractal. In addition, new bands were targeted including 900MHz cellular and 2.3GHz WiMax, both of which are in use in Canada.

The new layout, shown in Figure 55, includes changes to both characteristic line impedance and meander pattern. Though a curious-looking final result, the total area occupied by the antenna is 1377mm^2. This falls well within our target size of 3600mm^2 and represents a 53% decrease in overall size versus the previous antenna. This renders it a much better candidate for inclusion into small application circuits.

By incorporating the Koch meander pattern into the meandered stubs, it was possible to compact the stubs into less lateral width, thereby allowing the Koch loops to be drawn in closer and decreasing the total occupied area.

The total length for each of the loops was targeted at λ/2 ≈ 64.6mm at 881.7MHz, with feed lines of 5.6mm. From the re-arrangement of Equation 13:

$$L_{segment} = \frac{\left(L_{LoopTotal}\right) - 6\left(\frac{2\pi r}{3}\right) - 18\left(\frac{2\pi r}{6}\right)}{24}$$

$$L_{segment} = \frac{(64.6\text{mm}) - 6\left(\frac{2\pi(0.92mm)}{3}\right) - 18\left(\frac{2\pi(0.92mm)}{6}\right)}{24}$$

$$L_{segment} = 1.49mm$$

For the EM simulation, a deviation from this segment length was required due to impedance interactions with the open λ/4 stubs, Stub 1 and Stub 2. The width of these stubs was allowed to vary during an optimization routine in ADS. The changing characteristic impedance of the stub lines allowed a wider range of impedances to be presented to the main trace at the T-junctions. Although this eventually led to the addition of the 2.3GHz band, it came at the expense of heightening circuit Q and thereby reducing bandwidth in each of the frequency bands.

All pertinent dimensions in Figure 55 are provided in Table 9 for reference.

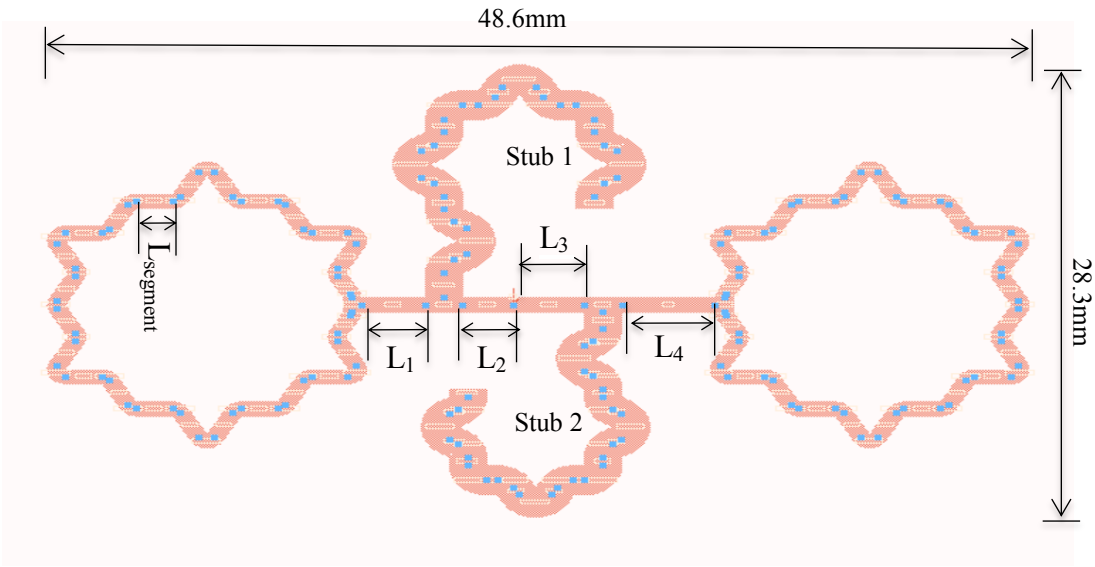

Figure 55 - Momentum Layout for Final Antenna

Table 9 - Summary of Microstrip Dimensions for Final Antenna

Measure	Value
$L_{segment}$	1.78mm = 70.1mils
L_1	3.12mm = 123mils
L_2	2.49mm = 98mils
L_3	3.45mm = 136mils
L_4	4.57mm = 180mils
W_{Stub1}	1.88mm = 74mil
L_{Stub1}	30.89mm = 1216mil
W_{Stub2}	1.9mm = 75mil
L_{Stub2}	27.1mm = 1066mil

As can be seen in Figure 56, acceptable return loss numbers were achieved for portions of the 850MHz and 900MHz (915MHz) cellular bands, as well as the 2.3GHz WiMax band. The 2.4GHz resonance observed during circuit simulation was not easily recovered after EM simulation and will be targeted in a future implementation.

The result nonetheless remains useful for three prominent Canadian frequency bands in a remarkably small occupied area.

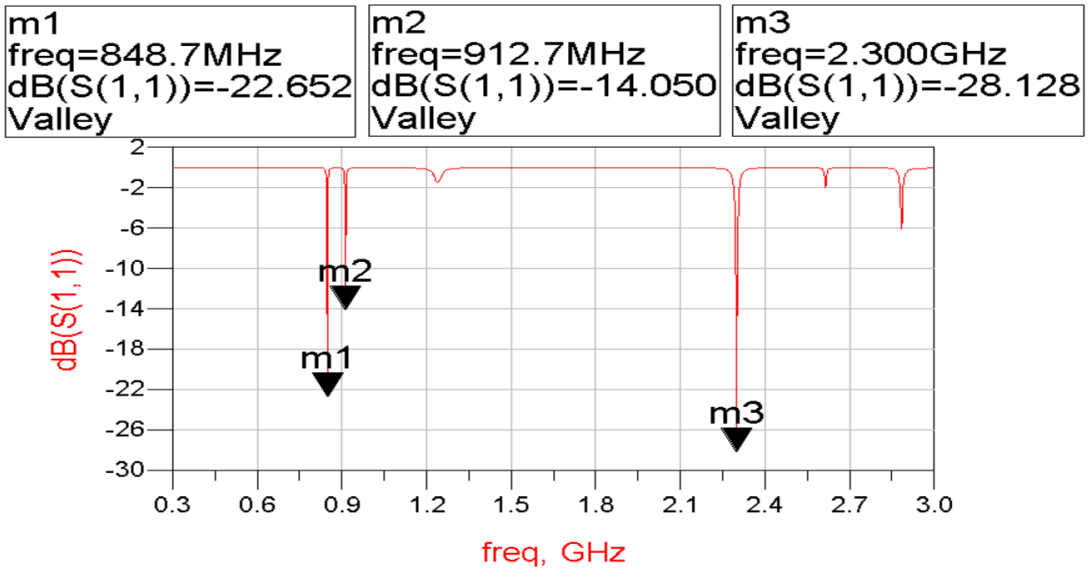

Figure 56 - Co-Simulated Return Loss Results for Final Antenna

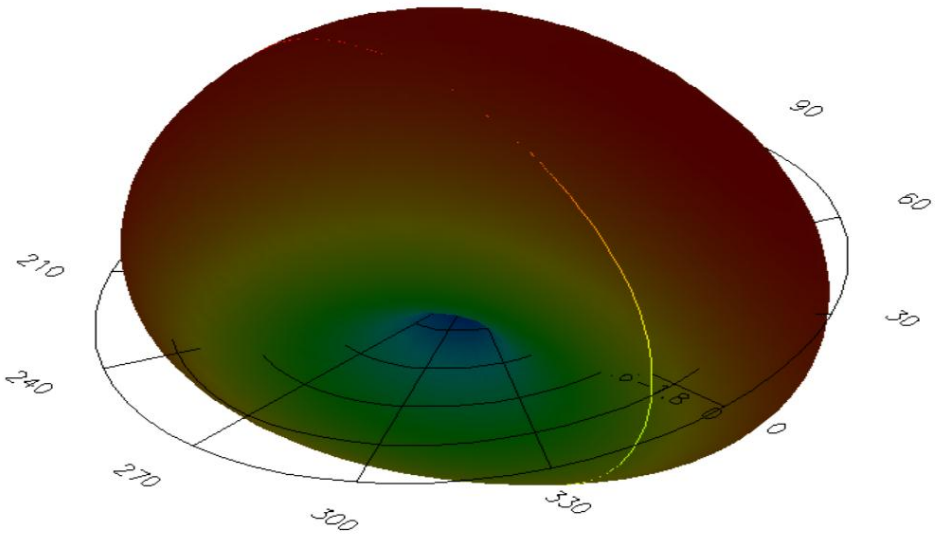

Figure 57 - Radiation Pattern (Final Antenna)

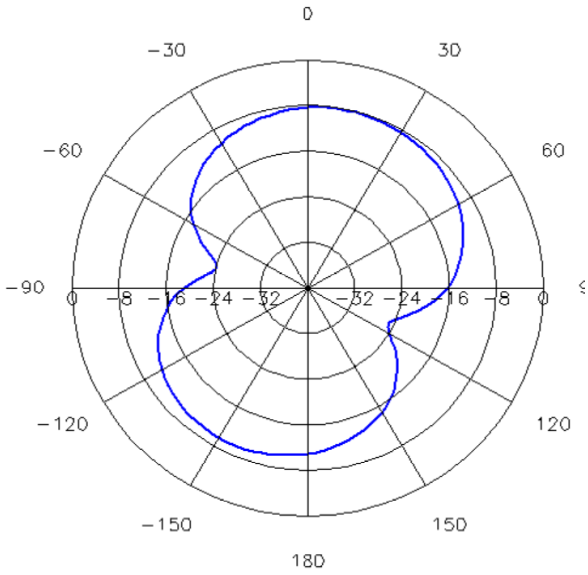

Figure 58 - Co-Polarization (ϕ=0°)

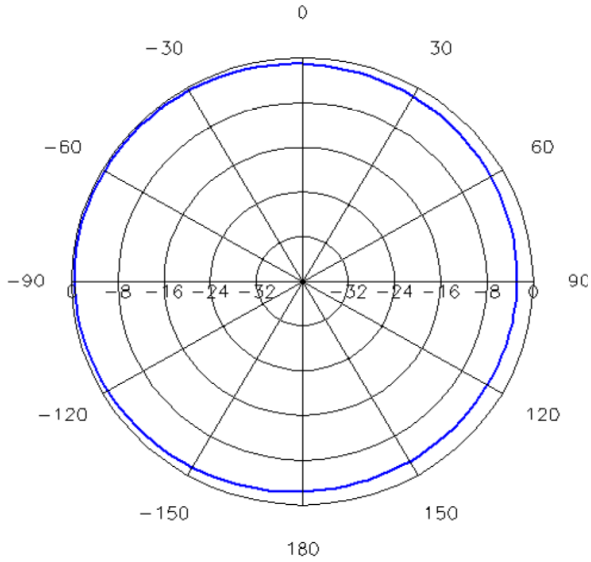

Figure 59 - Co-Polarization (ϕ=90°)

The radiation pattern, seen in Figure 57, remained generally omnidirectional, though a polar representation of the data shows a slight offset in the broadside radiation direction and more pronounced nulls at the angles perpendicular to this main lobe. The generally omnidirectional result is desirable for the intended personal consumer device application.

The complete power harvester circuit would include the antenna in Figure 55, the 7-element Greinacher rectifier in and the supercapacitor charge storage element described in Section 4.1.3. The combination is a three-layer board, with the antenna on the upper layer, a ground plane center layer and the rectifier and charge storage elements on the bottom layer. The connection from antenna to rectifier is made by a plated through via (insulated from the ground layer) from top layer to bottom layer. The charge storage element is fed from the rectifier and grounded at its other terminal by a *blind* via[20]. The connections are shown in Figure 60.

[20] While a *through* via connects the bottom and top layers and traverses the entire thickness of a PCB, a *blind* via only touches one of the two outer layers and 'ends' at some internal layer. In this case, an observer could not see through the board by looking at the via and thus the via is 'blind'.

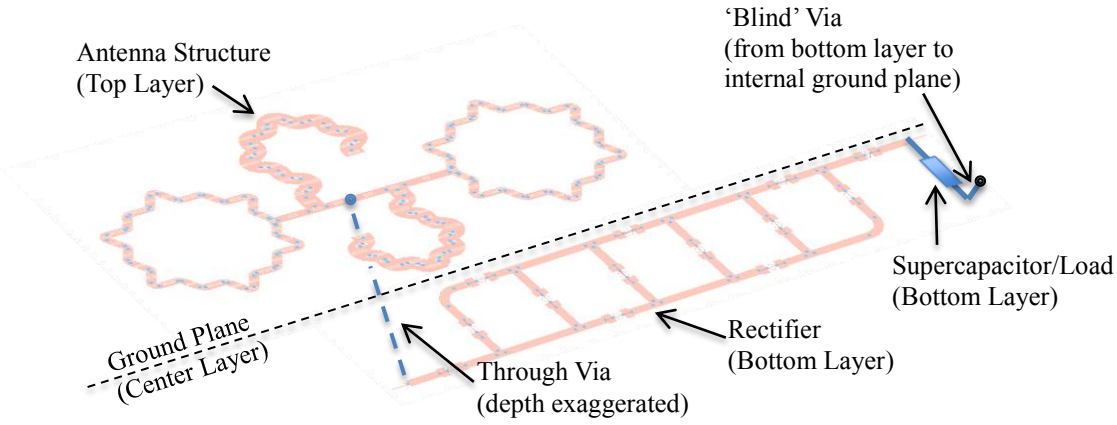

Figure 60 – 3-Layer Combination of RF Energy Harvester Elements

There are improvements to be brought to the simulation prior to manufacturing a complete circuit, including modelling of both vias, verification of unintended interactions between antenna and rectifier and modelling of interactions with surrounding elements in a sensor or calculator implementation.

4.3 – Conclusion

In this chapter, both a seven-element Greinacher rectifier and several microstrip antennas were designed and simulated with Agilent's ADS software package, resulting in the creation of all required components for a multi-band RF energy harvesting circuit for the cellular (850MHz), PCS (1900MHz) and WiMax (2.3GHz) bands. The rectifier circuit was able to achieve a peak PAE of 26.44%. The evolution of the antenna to a multi-pronged, multi-frequency Koch loop and meandered open stub antenna added operating frequencies and enhanced useable bandwidth. The final iteration reduced the antenna's occupied area by 53% via Koch transformations applied to the meandered stubs and further circuit compression.

Chapter 5 – Conclusions and Future Work

5.1 Conclusions

In this work, both a seven-element Greinacher rectifier and several microstrip antennas were designed and simulated with Agilent's ADS software package, resulting in the creation of all required components for a multi-band RF energy harvesting circuit for the cellular (850MHz and 900MHz), PCS (1900MHz), WiMax (2.3GHz) and Wi-Fi (2.4GHz) bands.

Contributions include simulations of an adapted Koch fractal loop antenna, an optimized Greinacher rectifier and a combined source-pull-based rectenna design approach. When compared to other recent constructed works in the area (summarized in Table 1), the power added efficiency (PAE) of 26%, occupied space (4.8cm x 2.8cm) and output level (-15.74dBm) are encouraging results. This being said, this work contributes the combination of the 850MHz, 900MHz, 1900MHz, 2.3GHz and 2.4GHz bands for exploitation in an RF energy-harvesting circuit, making it a highly interesting design for the Canadian/North American market.

Practical implementation challenges to consider include the physical link from antenna to rectifier (a through via), which will introduce parasitic elements and impedance change. Further to this are the circuit interactions with other physical elements of the consumer device in question, be they the device enclosure, other printed circuit boards in close proximity or mounting hardware, such as screws or rivets. Any of these elements could negatively affect performance if left unaddressed.

5.2 Future Work

Clear paths for future investigations include the addition of supplementary antennas at other operational frequencies and the further reduction of circuit size for incorporation into

common handheld devices. In addition, the match Q factor was high for the final design and thus optimal bandwidth was not achieved. This would a performance improvement target for future works.

To improve simulation accuracy, the full 'Three-Branch Equivalent Circuit' proposed for the supercapacitor in [43] will be used. This will introduce a voltage-dependant capacitance to model transients as energy is received. Further to this, more complete models for coupling capacitors and SMA connectors should be added to take package parasitics into account.

The integration of resistor emulation ([4],[36]) into the circuit would enhance the usability of the design over a wider range of input power levels, as per the expected conditions in a metropolitan area.

Further to this, some works have explored the use of deliberately defected ground structures (DGS) to alter antenna performance [50]. This can often be used to optimize frequency response and return loss within smaller physical areas by changing the effective impedance of the overlying microstrip line, thus requiring less copper to achieve a given characteristic impedance. These alterations fall outside the scope of the current paper, but the concept does relate in some small way to the mirrored antenna mentioned in [32], as there is no solid ground plane between the mirrored images, but rather a pairing of interdependent radiators that will invariably affect each other's radiation pattern and performance. This factor could be used as design criteria early in synthesis for new development.

References

[1] H.J. Visser, A.C.F. Reniers, J.A.C. Theeuwes, "Ambient RF Energy Scavenging: GSM and WLAN Power Density Measurements," IEEE, 38th European Microwave Conference, 2008. EuMC 2008. Amsterdam, Netherlands. pp. 721-724, October 27-31, 2008. ISBN: 978-2-87487-006-4

[2] W.C. Brown, "The History of Power Transmission by Radio Waves," IEEE Transactions on Microwave Theory and Techniques, vol. MTT-32, pp.1230-1242, Sept. 1984, doi: 10.1109/TMTT.1984.1132833

[3] M. Arrawatia, M.S. Baghini, G. Kumar, "RF Energy Harvesting System at 2.67 and 5.8GHz," IEEE Asia-Pacific Microwave Conference Proceedings, Yokohama, pp. 900-903, December 7–10, 2010, ISBN: 978-1-4244-7590-2

[4] M. Arrawatia, M.S. Baghini, G. Kumar, "RF Energy Harvesting from Cell Towers in 900MHz Band," IEEE, National Conference on Communications (NCC), Bangalore, pp. 1-5, January 28-30, 2011. ISBN: 978-1-61284-090-1

[5] D. Bouchouicha, M. Latrach, F. Dupont, L. Ventura, "An Experimental Evaluation of Surrounding RF Energy Harvesting Devices," IEEE, 40th European Microwave Conference Proceedings (2010), Paris, pp. 1381-1384, September 28-30, 2010. ISBN: 978-1-4244-7232-1

[6] A. Costanzo, F. Donzelli, D. Masotti, V. Rizzoli, "Rigorous Design of RF Multi-resonator Power Harvesters," IEEE, Proceedings of the Fourth European Conference on Antennas and Propagation (EuCAP 2010), Barcelona, pp. 1-4, April 12-16, 2010, ISBN: 978-1-4244-6431-9

[7] A. Georgiadis, G. Andia, A. Collado, "Rectenna Design and Optimization Using Reciprocity Theory and Harmonic Balance Analysis for Electromagnetic (EM) Energy Harvesting," IEEE Antennas and Wireless Propagation Letters, Vol.9, pp. 444-446, May 10, 2010, doi: 10.1109/LAWP.2010.2050131

[8] J.A. Hagerty, F.B. Helmbrecht, W.H. McCalpin, R. Zane, Z. Popovic, "Recycling Ambient Microwave Energy with Broad-Band Rectenna Arrays," IEEE Transactions

on Microwave Theory and Techniques, Vol. 52, No. 3, pp. 1014-1024, March 15, 2004, doi: 10.1109/TMTT.2004.823585

[9] U. Olgun, C.-C. Chen, J.L. Volakis, "Investigation of Rectenna Array Configurations for Enhanced RF Power Harvesting," IEEE Antennas and Propagation Letters, Vol. 10, pp.262-265, April 5, 2011, doi: 10.1109/LAWP.2011.2136371

[10] S.J. Orfanidis, "Electromagnetic Waves and Antennas," 2008, Rutgers University, Piscataway, New Jersey, USA, [Online], Available: http://www.ece.rutgers.edu/~orfanidi/ewa/ [Accessed April 2012]

[11] S. Rivière, A. Douyère, F. Alicalapa, J.D. Lan Sun Luk, "Study of Complete WPT System for WSN applications at Low Power Level," Electronics Letters, Institution of Engineering and Technology, University of la Reunion, Saint-Denis, France, 2010, Vol. 46, Issue 8, pp. 597-598, April 15, 2010, doi: 10.1049/el.2010.3063

[12] V. Rizzoli, D. Mascotti, N. Arbizzani, and A. Costanzo, "CAD Procedure for Predicting the Energy Received by Wireless Scavenging Systems in the Near- and Far-field Regions," IEEE Microwave Symposium Digest (MTT-S International), Bologna, pp.1, May 23-28, 2010, doi: 10.1109/MWSYM.2010.5515725

[13] T. Ungan, L.M. Reindl, "Harvesting Low Ambient RF-Source for Autonomous Measurements Systems," IEEE International Instrumentation and Measurement Technology Conference Proceedings, Victoria, Canada, pp. 62-65, May 12-15, 2008. ISBN: 978-1-4244-1540-3

[14] H. Jabbar, Y.S. Song, T.T. Jeong, "RF Energy Harvesting System and Circuits for Charging of Mobile Devices," IEEE Transactions on Consumer Electronics, Vol. 56, Issue 1, pp. 247-253, February 2010, doi: 10.1109/TCE.2010.5439152

[15] M. Mi, M.H. Mickle, C. Capelli, H. Swift, "RF Energy Harvesting with Multiple Antennas in the Same Space," IEEE Antennas and Propagation Magazine, Vol. 47, No. 5, pp. 100-106, October 2005, doi: 10.1109/MAP.2005.1599171

[16] T. Salter, G. Metze, N. Goldsman, "Parasitic Aware Optimization of an RF Power Scavenging Circuit with Applications to Smartdust Sensor Networks," IEEE Radio and Wireless Symposium 2009, San Diego, pp. 332-335, May 19, 2009, ISBN: 978-1-4244-2698-0

[17] T.S. Salter Jr., G. Metze, N. Goldsman, "Improved RF Power Harvesting Circuit

Design," International Semiconductor Research Symposium Proceedings, College Park, MD, USA, pp.1-2, December 12-14 2007, ISBN: 978-1-4244-1892-3

[18] M. Muramatsu, H. Koizumi, "An Experimental Result Using RF Energy Harvesting Circuit with Dickson Charge Pump," IEEE International Conference on Sustainable Energy Technologies (ICSET)2010, Kandy, pp.1-4, December 6-9, 2010, ISBN: 978-1-4244-7192-8

[19] S.H. Nasab, M. Asefi, L. Albasha, N. Qaddoumi, "Investigation of RF Signal Energy Harvesting," Active and Passive Electronic Components Journal (Hindawi Publishing Corporation), Volume 2010, Article ID 591640, pp.1-7, October 2010, doi: 10.1155/2010/591640

[20] T. Salter, K. Choi, M. Peckerar, G. Metze, N. Goldsman, "RF Energy Scavenging System Utilising Switched Capacitor DC-DC Converter," Electronics Letters (Institution of Engineering and Technology, Maryland, USA), Vol. 45, Issue 7, pp. 374-376, March 26, 2009, doi: 10.1049/el.2009.0153

[21] Z.J. Wu, W.L. Biao, S.K. Yak, T.C. Ming, B.C. Chye, Y.K. Seng, D.M. Anh, "Wireless Energy Harvesting Using Serially Connected Voltage Doublers," Proceedings of the 2010 Asia-Pacific Microwave Conference, Yokohama, pp. 41-44, December 7-10, 2010, ISBN: 978-1-4244-7590-2

[22] J. Ayers, K. Mayaram, T.S. Fiez, "An Ultralow-Power Receiver for Wireless Sensor Networks," IEEE Journal of Solid-State Circuits, Vol. 45, Issue. 9, pp. 1759-1769, August 23, 2010, doi: 10.1109/JSSC.2010.2056850

[23] D.M. Pozar, *Microwave Engineering*, Third Edition, John Wiley and Sons Inc., 2005, ASIN: B008VR8UPQ

[24] H. Yan, J.G.M. Montero, A. Akhnoukh, L.C.N. De Vreede, J.N. Burghartz, "An Integration Scheme for RF Power Harvesting," Submission for IEEE Annual Workshop on Semiconductor Advances for Future Electronics and Sensors from Delft University of Technology, Netherlands, pp. 17-18, November, 27-28, 2005, [Online], Available: http://scholar.googleusercontent.com/scholar?q=cache:ZXI_Q5OkUfYJ:scholar.google.com/&hl=en&as_sdt=0,5&as_vis=1 [Retrieved May 2012]

[25] D. Guha, Y. M. M. Antar, *Microstrip and Printed Antennas – New Trends, Techniques and Applications*, First Edition, John Wiley & Sons Ltd., ©2011, ISBN:

9780470681923

[26] Z.W.Sim, R. Shuttleworth, B. Grieve, “Investigation of PCB Microstrip Patch Receiving Antenna for Outdoor RF Energy Harvesting in Wireless Sensor Networks”, 2009 IEEE Conference on Antennas & Propagation Proceedings, Loughborough, pp.129-132, 16-17 November 2009, doi: 10.1109/LAPC.2009.5352525

[27] T.Q.V. Hoang, A. Douyere, J-L. Dubard, J-D. Lan Sun Lunk, “TLM Design of a Compact PIFA Rectenna”, 2011 International Conference on Electromagnetics in Advanced Applications (ICEAA) Proceedings, pp. 508-511, September 12-16, 2011, doi: 10.1109/ICEAA.2011.6046393

[28] C.P. Baliarda, J. Romeu, A. Cardama, “The Koch Monopole: A Small Fractal Antenna,” IEEE Transactions on Antennas and Propagation, Vol. 48, No. 11, pp. 1773-1781, November 2000, doi: 10.1109/8.900236

[29] A. Lamecki, P. Debicki, “Broadband Properties of a Minkowski Fractal Curve Antenna,” 14th International Conference on Microwaves, Radar and Wireless Communications, Vol. 3, pp.785-788, MIKON, August 7, 2002, ISBN: 83-906662-5-1

[30] S.N. Shafie, I. Adam, P.J. Soh, “Design and Simulation of a Modified Minkowski Fractal Antenna for Tri-Band Application,” Fourth Asia International Conference on Mathematical/Analytical Modelling and Computer Simulation (AMS) Proceedings, Kota Kinabalu, Malaysia, pp. 567-570, June 21, 2010, ISBN: 978-1-4244-7196-6

[31] E.W. Weisstein, “Minkowski Sausage,” MathWorld--A Wolfram Web Resource. [Online], Available from http://mathworld.wolfram.com/MinkowskiSausage.html [Retrieved April 2012]

[32] J. Zhou, Y. Luo, B. You, X.J. Yan, “Novel Tri-Band Antenna End-Loaded with Koch Fractal Loops,” Wiley Periodicals: Microwave and Optical Technology Letters, Vol. 54, No. 3, pp. 620-623, March, 2012, doi: 10.1002/mop.26657

[33] S.R. Best, “A Comparison of the Performance Properties of the Hilbert Curve Fracctal and Meander Line Monopole Antennas”, Wiley Periodicals: Microwave and Optical Technology Letters, Vol. 35, No. 4, pp. 258-262, November 2002, doi: 10.1002/mop.10576

[34] S.R. Best, “On the Multiband Behavior of the Koch Fractal Monopole Antenna”, Wiley Periodicals: Microwave and Optical Technology Letters, Vol. 35, No. 5, pp. 371-374,

December 2002, doi: 10.1002/mop.10610

[35] P. Zhao, Y. Zheng, M. Glesner, "Automatic Impedance Matching in Microwave Power Harvesters," Proceedings from 2010 Conference on Ph.D. Research in Microelectronics (PRIME), Berlin, pp.1-4, July18-21 2010. ISBN: 978-1-4244-7905-4

[36] T. Paing, J. Shin, R. Zane, Z. Popovic, "Resistor Emulation Approach to Low-Power RF Energy Harvesting," IEEE Transactions on Power Electronics, Vol.23. Issue 3, pp.1494-1501, May 2008, doi: 10.1109/TPEL.2008.921167

[37] A. S. Sedra, K.C. Smith, *Microelectronic Circuits*, Fourth Edition, Oxford University Press, 1998, pp. 197-198, ISBN: 0-19-511663-1

[38] D. Masotti, A.Constanzo, S. Adam, "Design and Realization of a Wearable Multi-Frequency RF Energy Harvesting System," 5th European Conference on Antennas and Propagation (EUCAP) Proceedings, Rome, pp.517-520, April 11-15, 2011, ISBN: 978-1-4577-0250-1

[39] T. Szepesi, K. Shum (Analog Devices), "Cell Phone Power Management Requires Small Regulators with Fast Response," EE Times News and Analysis. February 2002. [Online] Available at http://www.eetimes.com/electronics-news/4164128/Cell-phone-power-management-requires-small-regulators-with-fast-response [Retrieved April 2012]

[40] Rogers Corporation, "RT/duroid® 6006/6010LM High Frequency Laminates Data Sheet Rev 1.60000," Advanced Circuit Materials Division, Chandler, AZ. Publication: #92-105. Revised 03/2011. [Online], Available at http://www.rogerscorp.com/documents/612/acm/RT-duroid-6006-6010-laminate-data-sheet , [Retrieved June 2012]

[41] G.-P. Bava, U. Pisani, V. Pozzolo, "Source Pull Technique at Microwave Frequencies", Electronics Letters (Politecnico di Torino, Dipartimento di Ellectronica, Torino, Italy), pp. 152-154, February 16, 1984, doi: 10.1049/el:19840102

[42] R.C. Hansen, R.E. Collin, *Small Antenna Handbook*, John Wiley & Sons Inc. / IEEE Press, 2011, ISBN: 9781118106860

[43] A.S. Weddell, G.V. Merrett, T.J.Kazmierski, B.M.El-Hashimi, "Accurate Supercapacitor Modeling for Energy Harvesting Wireless Nodes," IEEE Transactions on Circuits and Systems-II: Express Briefs, Vol.58, No.12, pp.911-915, December

2011, doi:10.1109/TCSII.2011.2172712

[44] Agilent Technologies Inc., *stab_fact()*, Advanced Design System 2008 Documentation, Updated version available from http://www.home.agilent.com/en/pd-1374548/ads-2008?nid=-34346.870704.00&cc=CA&lc=eng

[45] G.E. Ponchak, "The Use of Metal Filled Via Holes for Improving Isolation in LTCC RF and Wireless Multichip Packages", IEEE Transactions on Advanced Packaging, Vol. 23, Issue 1, pp. 88-99, February 2000, doi: 10.1109/6040.826766

[46] G. Delisle, D. J. van Rensburg, D. McNamara, *Microwave Antenna Design, Testing and Wireless Propagation,* Electromagnetic Measurement Consultants Short Course Notes, The School of Information Technology and Engineering, University of Ottawa, ON, Canada, May 2009, (Unpublished)

[47] A. Kansal, J. Hsu, M. Srivastava, V. Raghunathan, "Harvesting Aware Power Management for Sensor Networks," Proceedings from 43rd ACM/IEEE Design Automation Conference, San Francisco, pp.651-656, July 24-28, 2006, doi: 10.1109/DAC.2006.229276

[48] C.-C. Lin, H.-R. Chuang, Y.-C. Kan, "A 3-12 GHz UWB Planar Triangular Monopole Antenna with Ridged Ground-Plane," Progress In Electromagnetics Research (PIER), Vol. 83, pages 307-321, 2008, doi: 10.2525/PIER08070502

[49] J.C. Lin, "Radio Frequency Exposure and Safety Associated with Base Stations Used for Personal Wireless Telecommunication," IEEE Antennas and Propagation Magazine, Vol. 44, Issue 1, pp.180-183, February 2002, doi: 10.1109/74.997962

[50] H.D. Oskouei, K. Forooraghi, M. Hakkak, "Radiation Characteristics of a Microstrip Patch Antenna over a Periodic Defected Ground Structure Substrate," Electromagnetics (January 2009), Volume 29, Issue 1, pp. 24-30, Dept. of Electrical Engineering, Tarbriat Modares University, Tehran, doi: 10.1080/02726340802529601

[51] M.V. Rusu, R. Baican, *Microwave and Millimeter Wave Technologies: from Photonic Bandgap Devices to Antenna and Applications,* Fractal Antenna Applications, (pages 351-382), March 2010, ISBN: 978-953-7619-66-4

[52] F. Iannello, O. Simeone and U. Spagnolini, "Energy Management Policies for Passive RFID Sensors with RF-Energy Harvesting," IEEE International Conference on Communications (ICC) Proceedings, Cape Town, pp.1-6, May 23-27, 2010, ISBN:

978-1-4244-6402-9

[53] S.M. Wentworth, *Fundamentals of Electromagnetics with Engineering Applications,* 1st Edition, John Wiley and Sons Inc., ©2005, ISBN: 0-471-26355-9

Appendix A – Microstrip design equations

The values in Table 4 were calculated from the well-published ([23], [53]) equations for microstrip effective permittivity, characteristic impedance and wavelength:

For the case of W < H

(i.e. a 50Ω line width, using RT/duroid 6010.2LM with 25mil substrate thickness):

$$\varepsilon_{eff} = \frac{\varepsilon_r + 1}{2} + \frac{\varepsilon_r - 1}{2}\left[\frac{1}{\sqrt{1 + 12\left(\frac{H}{W}\right)}} + 0.4\left(1 - \frac{W}{H}\right)^2\right]$$

$$Z_0 = \frac{120\pi}{\sqrt{\varepsilon_{eff}\left[\frac{W}{H} + 1.393 + \frac{2}{3}ln\left(\frac{W}{H} + 1.444\right)\right]}}\Omega$$

For the case of W ≥ H

(i.e. a 50Ω line width, using FR-4 with 25mil substrate thickness):

$$\varepsilon_{eff} = \frac{\varepsilon_r + 1}{2} + \frac{\varepsilon_r - 1}{2\sqrt{1 + 12\left(\frac{H}{W}\right)}}$$

$$Z_0 = \frac{120\pi}{\sqrt{\varepsilon_{eff}\left[\frac{W}{H} + 1.393 + \frac{2}{3}ln\left(\frac{W}{H} + 1.444\right)\right]}}\Omega$$

In case we are seeking a particular Z_0=50Ω, we can re-arrange the above equations, as shown in [53]. For the case of (*W/H*) ≤2, which covers both of the design, scenarios above, we have an approximation given by:

$$\frac{W}{H} = \frac{8}{e^{A} - 2e^{-A}}$$

where

$$A = \pi\sqrt{2(\varepsilon_r + 1)}\frac{Z}{\eta_0} + \frac{\varepsilon_r - 1}{\varepsilon_r + 1}\left(0.23 + \frac{0.11}{\varepsilon_r}\right)$$

Further precision is achieving by plugging the result into the rigorous equations proposed by Hammerstad and Jensen and re-published in [10]. Firstly to calculate the effective permittivity, we have:

$$\varepsilon_{eff} = \frac{\varepsilon_r + 1}{2} + \frac{\varepsilon_r - 1}{2}\left(1 + \frac{10}{u}\right)^{-ab}$$

where

$$a = 1 + \frac{1}{49}ln\left[\frac{u^4 + \left({}^{u}/_{52}\right)^2}{u^4 + 0.432}\right] + \frac{1}{18.7}ln\left[1 + \left(\frac{u}{18.1}\right)^3\right]$$

$$u = \frac{w}{h}$$

$$b = 0.564\left(\frac{\varepsilon_r - 0.9}{\varepsilon_r + 3}\right)^{0.053}$$

From these results, we calculate:

$$Z = \frac{\eta_0}{2\pi\sqrt{\varepsilon_{eff}}} ln\left[\frac{f(u)}{u} + \sqrt{1 + \frac{4}{u^2}}\right]$$

$$f(u) = 6 + (2\pi - 6)exp\left[-\left(\frac{30.666}{u}\right)^{0.7528}\right]$$

To calculate effective width (W), compensating for finite copper thickness (t):

$$W = w + \frac{t}{\pi}\left[ln\left(\frac{2h}{t}\right) + 1\right]$$

Where *w* and *h* represent the *uncompensated* width of the microstrip line and substrate thickness, respectively.

Next, we need to determine the effective strip length to represent a given electrical wavelength. Unlike the characteristic impedance, this length will very significantly, proportionally with frequency, if the dielectric stack up and other microstrip conditions remain the same.

$$\lambda = \frac{C}{f\sqrt{\varepsilon_{eff}}}$$

Appendix B – Octave .m File for Super-capacitor Equivalent Impedance Calculation

```
########################################
# Combine simplified model impedances
# args: rs, cs, rp, frequency
# Zeq
#   /\  |
#   |   |
#   |   \
#   |   /  Rs
#   |   \
#   |   /
#   |   |
#   |   |--------
#   |   |       |
#   |  ---      \
#   |  ___ Cs   / Rp
#   |   |       \
#   |   |       /
#   |   |_______|
#   |   |
#   \/  |
########################################
function comb= zsc(rs,cs,rp,f)
zfund=rs+(j*2*pi*f*cs+(1/rp))^-1
z2=rs+(j*2*pi*2*f*cs+(1/rp))^-1
z3=rs+(j*2*pi*3*f*cs+(1/rp))^-1
z4=rs+(j*2*pi*4*f*cs+(1/rp))^-1
z5=rs+(j*2*pi*5*f*cs+(1/rp))^-1
endfunction
```